

Broadband surface phonon spectroscopy by time-domain extreme ultraviolet diffuse scattering

F.Capotondi^{1,*}, A.Maznev², F.Bencivenga¹, S.Bonetti³, D.Fainozzi¹, D.Fausti¹, L.Foglia¹, C.Gutt⁴, N.Jaouen⁵, D.Ksenzov⁴, C.Masciovecchio¹, K.A.Nelson², I.Nikolov¹, M.Pancaldi^{1,3}, E.Pedersoli¹, B.Pfau⁶, L.Raimondi¹, F.Romanelli⁷, R.Totani¹, M. Trigo⁸

¹*Eletra Sincrotrone Trieste, Strada Statale 14, km 163.5, 34149 Basovizza, TS, Italy.*

²*Massachusetts Institute of Technology Cambridge, Massachusetts 02139, USA.*

³*Department of Molecular Sciences and Nanosystems, Ca' Foscari University of Venice, Venice, Italy*

⁴*Universität Siegen, Walter-Flex-Strasse 3, 57072 Siegen, Germany.*

⁵*Synchrotron SOLEIL, Saint-Aubin, Boite Postale 48, 91192, Gif-sur-Yvette Cedex, France.*

⁶*Max Born Institute, Max-Born-Straße 2A, 12489 Berlin, Germany.*

⁷*Department of Mathematics and Geosciences, University of Trieste, Trieste, Italy*

⁸*SLAC National Accelerator Laboratory, Menlo Park, CA, USA.*

We present experimental evidence that the dynamics of surface acoustic waves, with wavelengths ranging from tens to hundreds of nanometers, are encoded in the time-dependent diffuse scattering of extreme ultraviolet light. By measuring the diffuse scattering from a surface after an ultrafast optical excitation, we determined the dispersion relation of surface acoustic wave-packets across a broad range of wavevectors in various samples. The comparison of the signal amplitudes from samples with different surface morphologies suggests that the underlying excitation mechanism is related to the natural roughness of the samples surface. This simple and contactless approach represents a complementary experimental tool to transient grating or Brillouin spectroscopy, providing valuable insights into nanoscale surface dynamics.

Surface acoustic waves (SAWs) propagating at solid surfaces are important in many areas of human endeavor, ranging from seismology to the SAWs filter technology widely used in telecommunication devices. The interaction of light with the thermal population of surface acoustic phonons results in the phenomenon of surface Brillouin scattering, extensively used for the characterization of near-surface elastic properties [1,2]. While surface Brillouin spectroscopy has so far been restricted to the optical range, a nonlinear technique, referred to as transient grating (TG), has recently been extended to the extreme ultraviolet (EUV), enabling the generation of spatially periodic modulations of light intensity with a few tens of nm periods [3,4]. Such light patterns can then be used to excite and detect SAWs at nanoscale wavelengths [5,6]. Nanoscale SAWs can also be generated by optical laser irradiation of nanoscale periodic patterns fabricated on the sample surface [7,8] or through interdigital piezoelectrical transducer [9,10]. Thus, it would seem that patterning of either the radiation profile, as in the TG technique, or the sample is necessary for the excitation of coherent short wavelengths surface acoustic excitations.

In this letter, we report the unexpected observation of the generation of spatially random, but temporally coherent, nanoscale SAWs by unstructured femtosecond optical laser irradiation of an unpatterned sample surface. The scattering of a time-delayed EUV probe pulse by this surface excitation results in a pronounced dynamical circular fringe pattern in the EUV diffuse scattering (EDS). This fringe pattern evolves as a function of the pump-probe time delay with a well-defined group velocity, meaning that, at each point on the area detector, the EDS intensity oscillates at the SAW frequency corresponding to the wavevector defined by the scattering angle. This phenomenon is observed on multiple samples, including metals and semiconductors, bulk samples, thin films and multilayers, indicating a universal mechanism applicable to any sample that absorbs the optical pump pulse. By comparing samples with different surface morphology, we identify the sample roughness as the culprit responsible for the nanoscale SAWs excitation. The static scattering from surface roughness also provides a “local oscillator” field, essential for the

homodyne enhancement of the time-dependent observed circular fringe pattern. Our results provide the basis for a broad-band SAW spectroscopy tool covering a technologically important wavevector range, not accessible to traditional scattering spectroscopy techniques and largely surpassing EUV TG in terms of efficiency and easiness of practical realization. Developing a multiplexing approach at EUV wavelengths for nanoscale SAW spectroscopy could significantly impact several cutting-edge research areas, such as the functionalization of thin films to tailor specific performances within confined active areas of devices. This technology is crucial for precisely defining electronic, mechanical, and magnetic properties through the sequential deposition of ultrathin layers made from various materials. As the importance and complexity of advanced coatings and films increase, accurately characterizing their physical properties becomes increasingly essential. For example, the nanoscale elastic properties of thin layers significantly influence thermal conductivity, heat capacity and hardness [11,12] as well as the magnetic properties through spin-phonon coupling [13,14] and magnons emission [15,16,17]. Additionally, on the basis of our findings, the reported phenomenon will be present in any optical pump/EUV diffuse scattering probe measurement done in the reflection geometry, therefore one needs to be aware of the effect for a correct interpretation of experimental data involving different degree of freedom, such as, for example, magnetic excitations in tens of GHz regime [18,19].

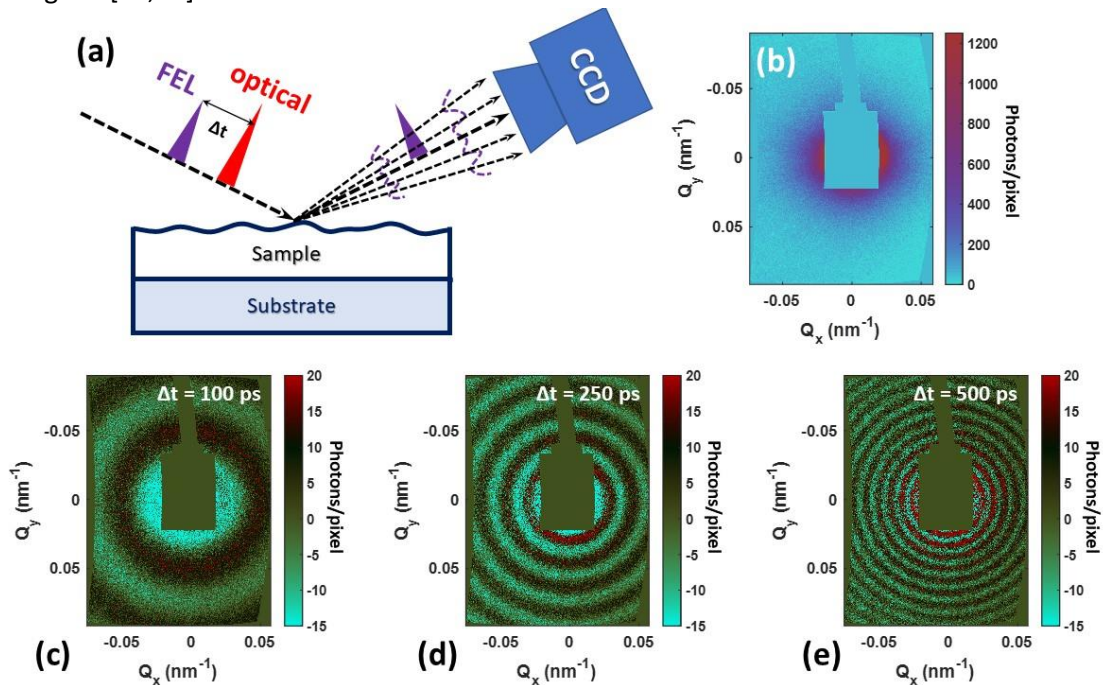


Figure 1. (a) A coherent FEL pulse impinges on the sample surface at an incident angle of 45° . A collinear optical pulse, advanced by Δt , is used to excite the SAWs. The diffuse scattering, resulting from the interference between the scattering caused by surface roughness and the surface displacement induced by the SAWs, is collected by a CCD detector. (b) Typical static EDS intensity at the detector for a $[\text{Pt}(4\text{nm})/\text{Al}(4\text{nm})]_4$ multilayer stack grown on a Si/SiO₂ substrate. The central shadowed region in the image represents missing data due to the beamstop blocking the specularly reflected beam. (c) - (e) Differential EDS images, $\Delta I_{EDS}(Q_x, Q_y, \Delta t)$, recorded at 100 ps, 250 ps and 500 ps after the optical stimulus, revealing a ring-like dynamic pattern in the EDS intensity variation.

The experiment was conducted at the DiProI end station of the FERMI FEL facility in Trieste, Italy. Figure 1(a) illustrates the layout of the experiment setup. The sample surface is oriented at approximately 45° with respect to the optical-FEL pulse sequence. The diffuse scattering of a monochromatic FEL pulse ($\lambda_{\text{FEL}} = 17.8$ nm, pulse duration 50 fs, bandwidth $\Delta\lambda_{\text{FEL}}/\lambda_{\text{FEL}} = 2 \times 10^{-3}$), focused to a spot size of about $150 \times 120 \mu\text{m}^2$, is recorded by a CCD detector positioned 50 mm from the interaction point. To trigger the lattice dynamics, a nearly collinear optical pulse ($\lambda_{\text{opt}} = 395$ nm, pulse duration 80 fs) is focused on the same location as the

FEL probe beam, delivering a power density between 8 and 30 mJ/cm² into a spot size of about 300x250 μm². During the experiment, the FEL probe energy density was set to about 1.5 mJ/cm² and the relative delay (Δt) between the two pulses was varied up to 1 ns. Figure 1 (b) shows an example of static featureless EDS intensity, $I_{EDS}(Q_x, Q_y)$, from a [Pt(4 nm)/Al(4 nm)]_{x4} multilayer stack deposited on Si/SiO₂ substrate. In this image, Q_x and Q_y represent the orthogonal components of the exchanged momentum ($Q = \sqrt{Q_x^2 + Q_y^2}$) in the detector plane. In the experiment, the detector was exposed to 600 FEL shots at a 50 Hz repetition rate. After optical pumping, significant variations — up to a few percent — in the pumped $I_{EDS}(Q_x, Q_y, \Delta t)$ intensity are clearly observable in the differential image $\Delta I_{EDS}(Q_x, Q_y, \Delta t)$, which is defined as follows:

$$\Delta I_{EDS}(Q_x, Q_y, \Delta t) = (I_{EDS}(Q_x, Q_y, \Delta t) - I_{EDS}(Q_x, Q_y)) \quad (1)$$

where $I_{EDS}(Q_x, Q_y)$ represents the static reference EDS intensity collected without applying optical laser pumping. The Figures 1(c)-(e) show snapshots of $\Delta I_{EDS}(Q_x, Q_y, \Delta t)$ at three representative delays: 100 ps, 250 ps and 500 ps. A concentric ring structure is clearly visible at each delay, with an increasing number of maxima and minima as Δt progress. A full movie showing the time evolution of this fringe structure is available in the Supplementary Information file “EDSvsTime_movie.avi”. This ring-like pattern can result from the interference between the static diffuse scattering field due to surface roughness and the periodic, time-dependent and phase-locked modulation caused by a coherent surface displacement associated with SAWs. To investigate this hypothesis, Figure 2(a) presents the time evolution of the azimuthal radial average of the differential diffuse EDS intensity, defined as:

$$S(Q, \Delta t) = \int_0^{2\pi} \Delta I_{EDS}(Q, \phi, \Delta t) d\phi \quad (2)$$

where ϕ is the azimuthal angle in the detector plane. For a given Q , an oscillating behavior as a function of Δt is observed (see also Figure 2(b), where lineouts at selected Q in the range from 0.04 nm⁻¹ to 0.10 nm⁻¹ are displayed). The dynamical features observed in Figure 2(a) are similar to the two-dimensional maps of time-resolved impulsive Brillouin scattering from bulk samples probed by broadband optical pulses [20,21]. However, in this class of experiments, the underlying detection scheme relies on the interferometric modulation of the reflected intensity caused by strain packets propagating within the sample, which requires optically transparent materials and thus cannot be used to probe surface dynamics.

In Figure 2(c) we present the Fourier transform of Figure 2(a), revealing an excitation oscillation frequency that linearly disperses as a function of Q and extends up to 25 GHz. The slope of such a dispersion corresponds to a group velocity of $1.52 \pm 0.05 \times 10^3$ m/s, which is consistent with the velocity of the first Rayleigh surface mode of the stratified layered structure of the sample [21]. This observation rules out Brillouin scattering from bulk modes probed by EUV radiation as the primary source of the observed dynamics, since their recently reported frequency are in the 0.1-1.0 THz regime [22]. This finding suggests that the coherent modulations of surface displacements are responsible for the ring-like patterns observed in the diffuse scattering intensity. However, differently to ref. [23], the absence, in the experimental response, of a doubling of the phonon frequency excludes that the dynamics is related to squeezed phonon states lunched by the nearly instantaneous change of the electronic crystal field after optical excitation. Figure 2(d) shows the dependence of $S(Q, \Delta t)$ at $Q = 0.05$ nm⁻¹ on the optical laser fluence F_{ex} , ranging from 7.5 mJ/cm² to 30 mJ/cm². The data reveal a linear increase in the signal amplitude, as highlighted in Figure 2(e), which illustrates the peak amplitude of the Fourier transform of $S(Q = 0.05$ nm⁻¹, $\Delta t)$ as a function of F_{ex} . The linear dependence on F_{ex} at a given Q supports the interpretation that the observed fringe structure in the $\Delta I_{EDS}(Q_x, Q_y, \Delta t)$ pattern originates from dynamical light scattering of the EUV radiation by the SAWs. Indeed, if we assume that the observed time dependence in the EDS intensity, $I_{EDS}(t)$, results from the coherent sum of the static (time-independent) electric field scattered by the surface roughness (E_{SR}) and the time-dependent field due to SAW propagation ($E_{SAW}(t)$), we can write the EDS intensity as $I_{EDS}(t) = |E_{SR} + E_{SAW}(t)|^2$. Under the condition that the vertical displacement of the SAW (u_{SAW}) is much smaller

than the root-mean-square surface roughness (σ_R) [16] and assuming that the electric field amplitudes are linearly proportional to the surface phonon displacement u_{SAW} , it follows that $E_{SR} \gg E_{SAW}(t)$. Therefore, under a phase-locked condition between the fields E_{SR} and $E_{SAW}(t)$, the differential signal can be approximated at the first order as $\Delta I_{EDS}(t) \approx |E_{SR}| |E_{SAW}(t)| \cos(\varphi)$, which is linearly dependent on E_{SAW} and, consequently, on u_{SAW} . Since u_{SAW} scales linearly with the laser fluence F_{ex} , due to thermal expansion, a corresponding linear dependence of differential scattering amplitude, as shown in Figure 2(e), is expected. It is important to note that the assumption of a phase-locked condition between the E_{SR} reference field and the dynamical scattering $E_{SAW}(t)$ differs significantly from a recently reported effect observed in the hard X-ray regime [24]. In that case, the oscillatory behavior around a Bragg peak in reflection geometry is attributed to phonon propagation induced by the random absorption of high-energy photons, leading to localized thermal lattice expansion. However, a random absorption mechanism, i.e. a lacking of a fixed and constant phase relation between E_{SR} and $E_{SAW}(t)$, would result in signal cancellation in a multi-shot experiment like the one presented here. Moreover, such a mechanism would yield a quadratic dependence of the oscillatory amplitude on laser intensity, as the total signal would scale with the square of the number of absorption centers inside the material, a behavior clearly inconsistent with the trend observed in Figure 2(e).

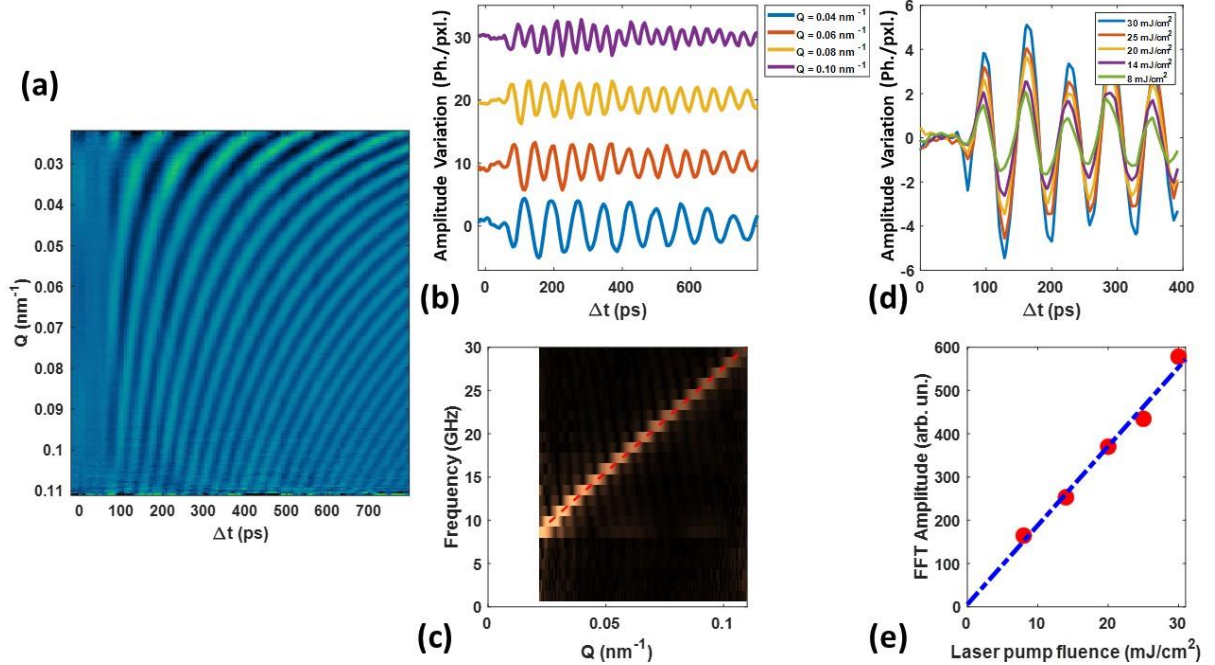


Figure 2. (a) Azimuthal radial average map $S(Q, \Delta t)$ as a function of Q and Δt for the [Pt(4nm)/Al(4nm)]₄ multilayer stack on a Si/SiO₂ substrate. (b) Time dependence of $S(Q, \Delta t)$ at selected values of Q in the range 0.03 – 0.09 nm⁻¹. (c) Fourier transform of the data in panel (a), with the dashed red line highlighting the linear dispersion of the oscillation frequency vs phonon wavevector (Q), corresponding to a velocity of the acoustic excitation of 1520 ± 50 m/s. (d) Time dependence of $S(Q, \Delta t)$ at $Q = 0.05$ nm⁻¹ as a function of the optical excitation fluence (F_{ex}). (e) Dependence of the peak amplitude of the Fourier transform on F_{ex} for $Q = 0.05$ nm⁻¹.

To assess the role of surface roughness in the generation of the SAW through the optical stimulus, we report in Figure 3 the results from Pt films (50 nm thick) deposited under identical conditions on different substrates. The surface quality of the substrate influences the nucleation phase of the Pt film during the initial deposition stages, leading to variations in the final surface morphology. Atomic force microscopy (AFM) of as-grown samples (Figure 2(a) and 2(c)) reveals a smoother surface and smaller grain size for Pt film grown on a Si substrate ($\sigma_R = 0.6$ nm, roughness correlation length of 10 ± 1 nm) compared to the film on a Si₃N₄ substrate ($\sigma_R = 1.1$ nm, roughness correlation length of 11 ± 2 nm). As a direct consequence of the higher surface roughness, for a given time delay ($\Delta t = 350$ ps) and excitation laser fluence ($F_{ex} = 10$ mJ/cm²), the

amplitude of the oscillations in the differential EDS signal is larger for the sample having the higher value of σ_R (Figure 2(e), see also the differential EDS images Figure 2(b) and 2(d)). As reported in Figure S10(c) and S12(c) of Supplementary Material, it's worth noting that for lower Q values ($Q < 0.06 \text{ nm}^{-1}$) the observed difference between the two samples response is mostly due to the predominant excitation of the second Rayleigh overtone by optical pulse for Pt layer grown on Si substrate.

The experimental observation of a correlation among the amplitude of differential EDS signal and the sample morphology supports the hypothesis that surface roughness drives the process of SAWs generation. We can identify two potential microscopic mechanisms responsible for the generation of a coherent broadband SAW excitation in materials. The first mechanism involves uneven laser energy deposition, which induces localized and non-uniform thermal strain at the surface, acting as a random source of mechanical perturbations that launch the observed broadband SAW spectrum. This process aligns with electromagnetic theories explaining the formation of laser-induced periodic surface structures, which emerge when the optical pulse intensity exceeds the material's damage threshold [25,26,27]. In this scenario, non-uniform laser absorption, even at spatial frequencies smaller than the optical laser wavelength, results from interference between the incident laser beam and near-field back reflections from irregular surface features. This near-field interference effect due to sample roughness guarantees a phase locked condition among different shots and, as previously discussed, a non-vanishing average of the homodyne detection signal with the reference field E_{SR} .

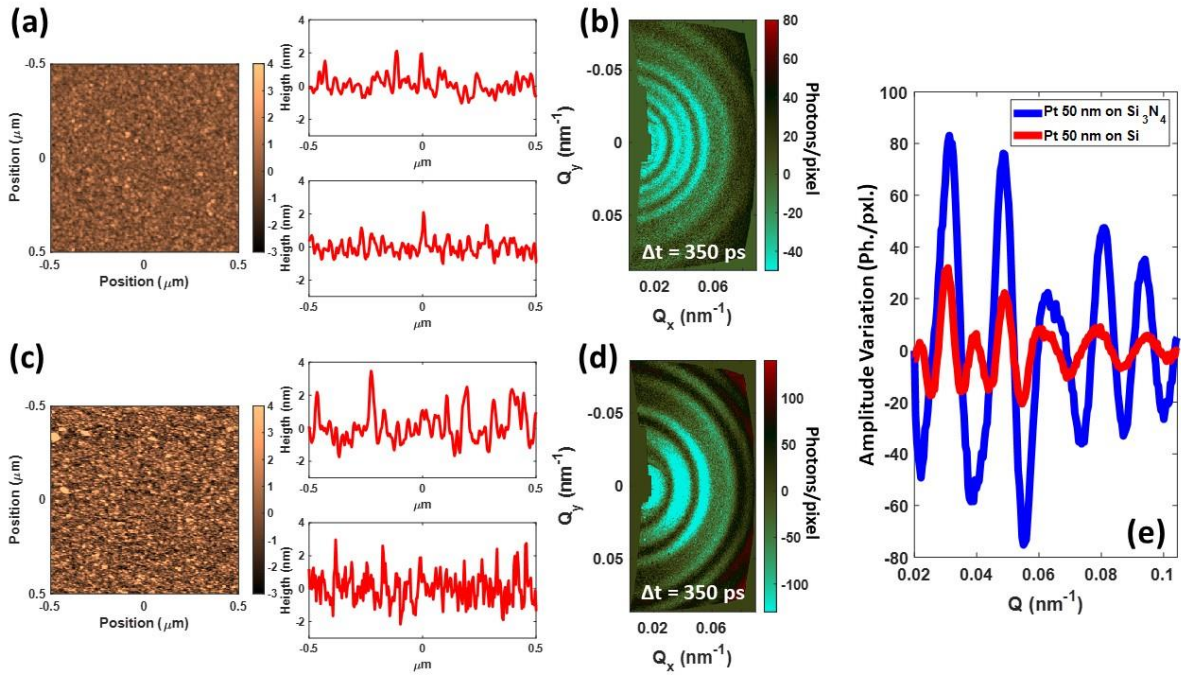


Figure 3. (a) AFM image (size $1 \times 1 \mu\text{m}^2$) and lineouts along orthogonal directions for a 50 nm thick Pt film grown on Si substrate. (b) Differential EDS images, $\Delta I_{EDS}(Q_x, Q_y, \Delta t)$, for Si/Pt sample recorded after 350 ps from an optical stimulus of 10 mJ/cm^2 . (c) AFM image (size $1 \times 1 \mu\text{m}^2$) and lineouts along orthogonal direction for a 50 nm thick Pt film grown on Si₃N₄ substrate. (d) Differential EDS images, $\Delta I_{EDS}(Q_x, Q_y, \Delta t)$, for Si₃N₄/Pt sample recorded after 350 ps from an optical stimulus of 10 mJ/cm^2 . (e) Differential EDS images, $\Delta I_{EDS}(Q_x, Q_y, \Delta t)$, for Si₃N₄/Pt sample recorded at 300 ps after the optical stimulus (deposited energy 10 mJ/cm^2). (e) Azimuthal average of the differential diffuse scattering intensity $S(Q, \Delta t)$ at $\Delta t = 350$ ps for the two samples, measured under identical experimental conditions with an optical excitation fluence $F_{ex} = 10 \text{ mJ/cm}^2$.

Alternatively, a broadband coherent surface phonon field can be generated through the conversion of longitudinal thermoelastic strain, induced by uniform laser absorption, into acoustic surface modes. This

occurs due to the non-specular reflection of acoustic energy at a rough surface [28]. As highlighted by A. Maznev in ref. [28], in the intermediate regime between the Rayleigh scattering limit (where the roughness correlation length is much smaller than the phonon wavelength) and the Kirchhoff approximation (which assumes a correlation length much greater than the acoustic wavelength) the probability of diffuse scattering of longitudinal acoustic waves into transverse and Rayleigh waves reaches its maximum.

To evaluate the general applicability of the observed dynamical effect, we repeated the experiment with different samples, including Co(75 nm)/Ta(2nm), Ti(100 nm), Ta(75 nm), Cr(7 nm)/Au(75 nm) thin film deposited on Si substrate as well as bulk crystal samples of Si, GaAs and Ge (001) oriented. As examples, Figures 4(a) and 4(d) show selected differential images of EDS after 200 ps from the optical excitation for (001) oriented GaAs crystal and for a 100 nm thick Ti film deposited on Si substrate, while Figures 4(b) and 4(e) show the respective $S(Q, t)$ maps. Despite the lower surface roughness of the GaAs crystal ($\sigma_R = 0.2$ nm, see also Figure S18 of Supplementary Material), a clear oscillatory behavior is observed across the entire probed Q -range, demonstrating the approach's reliability even for low-roughness samples. The Fourier transform of the $S(Q, t)$ map for GaAs, shown in Figure 4 (c), reveals a single phonon mode with a group velocity of $3.03 \pm 0.05 \times 10^3$ m/s, which is consistent with the Rayleigh wave velocity for bulk GaAs [29,30]. In contrast, the Fourier analysis of the $S(Q, t)$ map for the 100 nm Ti film, displayed in Figure 4(f), reveals additional vibration modes that disperse with Q , alongside the fundamental Rayleigh mode (indicated by the red dashed line in Figure 4(f)). The dispersion relations of these additional modes, known as Sezawa SAW modes, align well with theoretical predictions obtained by solving the Rayleigh equation for stratified media (green and magenta dashed lines) [21].

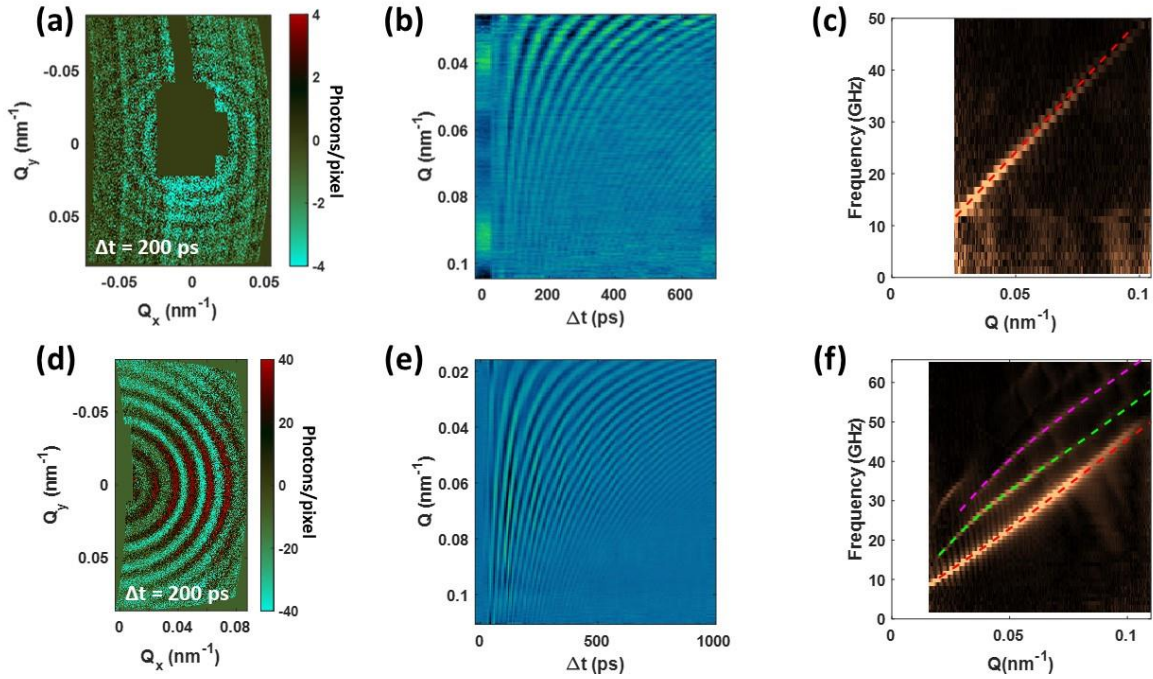


Figure 4. (a) and (d) Differential EDS images, $\Delta I_{EDS}(Q_x, Q_y, \Delta t = 200 \text{ ps})$, for a (001) oriented GaAs crystal and a 100 nm thick Ti layer on a Si substrate, respectively. (b) and (e) retrieved $S(Q, t)$ maps for the two samples. (c) Fourier transform of the map reported in panel (b), revealing the linear dispersion of Rayleigh acoustic waves with a velocity of approximately 3030 ± 50 m/s for (001) oriented GaAs crystal (dashed red line). (f) Fourier transform of the map reported in panel (e), displaying the excitation three modes, the fundamental Rayleigh wave and two overtones, for 100 nm thick Ti layer on a Si substrate. The dashed red, green, and magenta lines represent the calculated dispersion relations based on the Rayleigh equations for stratified media [21].

In all investigated samples (see Supplementary Material section S2 for detailed analysis of other samples studied during the experimental campaign), the dispersion relation was determined up to $Q \approx 0.11 \text{ nm}^{-1}$, corresponding to a SAW wavelength down to approximately 60 nm. However, we anticipate that SAWs

with even higher Q values could be excited and detected. The Q -range of this specific experiment is limited by the experimental geometry and detector size, which limits the range to well below the theoretical maximum value of Q , which is $Q_{max} = 4\pi \times \lambda_{FEL}$ dictated by the wavelength of the EUV probe and the maximum possible scattering angle (180°). In summary, our findings demonstrate that time-resolved EDS is a simple, reliable and versatile approach for probing surface phonon dynamics. It offers the significant advantage of accessing a broad wavevector range at nanoscale wavelengths within a single time-delay scan. This range can be substantially extended by employing an experimental geometry that accommodates larger scattering angles or by using a shorter probe wavelength, such as in the soft X-ray region. We have specifically observed acoustic Rayleigh modes, which induce coherent modulations of surface displacement across a wide variety of metallic and semiconductor materials. This suggests that this phenomenon generally occurs in any sample with non-zero surface roughness that can absorb the optical excitation pulse. Unlike conventional picosecond ultrasonic methods, our approach does not require the fabrication of tailored nanostructures to access nanoscale spatial wavelengths. This provides unique capabilities for investigating thermoelastic properties in a contactless manner on both thin films and bulk materials at the nanoscale [31,32]. In contrast to EUV transient grating, this approach overcomes the strict limitation of measuring only a single wavevector at a time [33,34], enabling straightforward detection of SAW mode dispersion relations with high precision. Moreover, the simplicity of the setup and the linearity of the experimental signal with EUV intensity suggest that this method could be implemented using table-top EUV sources. Typically, a total number of EUV photons in the range of 5×10^{12} - 5×10^{13} (see Supplementary Material Section S2, Table S1) was required to achieve a good signal-to-noise ratio in an EDS measurement. Given that state-of-the-art table-top sources can produce about 10^{12} - 10^{13} ph/s/eV [35], an acquisition time of just a few minutes would be sufficient to collect an EDS image with similar counting contrast and probing photons bandwidth ($\Delta\lambda/\lambda \sim 10^{-3}$). Additionally, the ability to determine SAW dynamics across a wide range of momentum transfers at the nanoscale is expected to provide critical insights into various aspects of material response. This capability, for instance, could significantly enhance the modeling of surface wave attenuation in the GHz regime enabling the discrimination between intrinsic processes, such as thermoelastic dissipation, Akhiezer damping, three-phonon anharmonic decay, and extrinsic factors like surface roughness, mass load, grain boundary scattering [28,36,37]. Such insights could greatly improve the tailoring of surface phonon properties for advanced applications, including telecommunication electronics [38], the stability of nanoelectromechanical systems [39] and chemical and biological mass detector sensing [40]. As a result, it could lead to a reduced power and an enhanced sensitivity in inertial sensors. Finally, since the EDS approach collects scattered photons at all azimuthal angles, we envision a straightforward extension of this methodology to the study of high-frequency magnon-SAW coupling [41], where the hybridization of magnon-phonon modes is maximized within a specific angular range between the propagation direction of the acoustic surface excitation and the external magnetic field [42,43].

References

-
- [1] S.B. Ross-Murphy *Dynamic light scattering*, B. J. Berne and R. Pecora, John Wiley, New York, 1976.
 - [2] R.Y. Chiao, C.H. Townes, B.P. Stoicheff, *Stimulated Brillouin scattering and coherent generation of intense hypersonic waves*, Phys Rev Lett. 12,592 (1964).
 - [3] F. Bencivenga, R. Cucini, F. Capotondi, et al., *Four-wave mixing experiments with extreme ultraviolet transient gratings*. Nature 520, 205–208 (2015). <https://doi.org/10.1038/nature14341>
 - [4] F. Bencivenga, R. Mincigrucci, F. Capotondi, et al., *NanoScale transient gratings excited and probed by extreme ultraviolet femtosecond pulses* Sci Adv. 5, eaaw5805, (2019).
 - [5] A.A. Maznev, F. Bencivenga, A. Cannizzo, et al. *Generation of coherent phonons by coherent extreme ultraviolet radiation in a transient grating experiment* Appl Phys Lett. 113, 221905 (2018).
 - [6] A.A. Maznev, R. Mincigrucci, F. Bencivenga, et al. *Generation and detection of 50 GHz surface acoustic waves by extreme ultraviolet pulses* Appl Phys Lett. 119, 044102 (2021).
 - [7] J.N. Hernandez-Charpak, K.M. Hoogetboom-Pot, Q. Li, et al., *Full characterization of the mechanical properties of 11–50 nm ultrathin films: influence of network connectivity on the Poisson's ratio*, Nano Lett. 17, 2178 (2017).

-
- [8] M.E. Siemens, Q. Li, M.M. Murnane, et al., *High-frequency surface acoustic wave propagation in nanostructures characterized by coherent extreme ultraviolet beams*, Appl. Phys. Lett. 94, 093103 (2009).
- [9] M.K. Ekström, T. Aref, J. Runeson, et al., *Surface acoustic wave unidirectional transducers for quantum applications*, Appl. Phys. Lett. 110, 073105 (2017).
- [10] M. J. A. Schuetz, E. M. Kessler, G. Giedke, et al., *Universal Quantum Transducers Based on Surface Acoustic Waves*, Phys. Review X 5, 031031 (2015). DOI: 10.1103/PhysRevX.5.031031
- [11] V. Chiloyan, S. Huberman, A. A. Maznev, et al., *Thermal transport exceeding bulk heat conduction due to nonthermal micro/nanoscale phonon populations*, Appl. Phys. Lett. 116, 163102 (2020).
- [12] J. Zhou, H. D. Shin, K. Chen, et al., *Direct observation of large electron–phonon interaction effect on phonon heat transport* Nat. Commun. 11, 6040 (2020).
- [13] J. Janušonis, T. Jansma, C. Chang, et al., *Transient Grating Spectroscopy in Magnetic Thin Films: Simultaneous Detection of Elastic and Magnetic Dynamics*. Sci Rep 6, 29143 (2016).
- [14] P. Carrara, M. Brioschi, E. Longo, et al., *All-Optical Generation and Time-Resolved Polarimetry of Magnetoacoustic Resonances via Transient Grating Spectroscopy*, Phys. Rev. Applied 18, 044009 (2022).
- [15] V. Temnov, *Ultrafast acousto-magneto-plasmonics*, Nature Photon 6, 728–736 (2012). <https://doi.org/10.1038/nphoton.2012.220>.
- [16] K. Baumgaert, J. Gräfe, P. Che, et al., *Nanoimaging of Ultrashort Magnon Emission by Ferromagnetic Grating Couplers at GHz Frequencies*, Nano Letters, 20, 7281–7286 (2020).
- [17] A. Mucchietto, K. Baumgaertl, and D. Grundler, *Magnon-Assisted Magnetization Reversal of Ni₈₁Fe₁₉ Nanostripes on Y₃Fe₅O₁₂ with different interfaces*, ACS Nano, 18, 8641–8648 (2024).
- [18] M. Geilen, R. Verba, A. Hamadeh, et al., *Parametric Excitation and Instabilities of Spin Waves Driven by Surface Acoustic Waves*, Adv. Physics Res., 4, 2400086 (2025).
- [19] Y. Hwang, J. Puebla, K. Kondou, et al., *Strongly Coupled Spin Waves and Surface Acoustic Waves at Room Temperature*, Phys. Rev. Lett. 132, 056704 (2024).
- [20] E. Pontecorvo, M. Ortolani, D. Polli, et al., *Visualizing coherent phonon propagation in the 100 GHz range: A broadband picosecond acoustics approach*, Appl. Phys. Lett. 98, 011901 (2011).
- [21] J.D. Achenbach, *Wave Propagation in Elastic Solids*, North Holland Publishing Co., New York (1973).
- [22] D. Fainozzi, L. Foglia, N.N. Khatu, et al., *Stimulated Brillouin scattering in the time domain at 1nm⁻¹ wave vector*, Phys. Rev. Lett. 132, 033802 (2024).
- [23] M. Trigo, M. Fuchs, J. Chen, et al., *Fourier-transform inelastic X-ray scattering from time- and momentum-dependent phonon–phonon correlations*, Nature Phys 9, 790–794 (2013). <https://doi.org/10.1038/nphys2788>
- [24] Y. Huang, P. Sun, S.W. Teitelbaum, et al., *Nanometer-Scale Acoustic Wave Packets Generated by Stochastic Core-Level Photoionization Events*, Phys. Review X 14, 041010 (2024). DOI: <https://doi.org/10.1103/PhysRevX.14.041010>
- [25] Jörn Bonse and Stephan Gräf, *Maxwell Meets Marangoni—A Review of Theories on Laser-Induced Periodic Surface Structures*, Laser Photonics Rev., 14, 2000215, (2020).
- [26] Hao Zhang, Jean-Philippe Colombier, and Stefan Witte, *Laser-induced periodic surface structures: Arbitrary angles of incidence and polarization states*, Phys. Rev. B 101, 245430 (2020).
- [27] J.Z.P. Skolski, G.R.B.E. Römer, J. V. Obona, et al., *Laser-induced periodic surface structures: Fingerprints of light localization*, Phys. Rev. B 85, 075320 (2012). DOI: <https://doi.org/10.1103/PhysRevB.85.075320>
- [28] A.A. Maznev, *Boundary scattering of phonons: Specularity of a randomly rough surface in the small-perturbation limit*, Physical Review B 91, 134306 (2015).
- [29] N. Tarasenko, P. Bohac, L. Jastrabik, et al., *Effect of roughness on the phase velocity of Rayleigh waves in GaAs crystals*, Thin Solid Films 491, 184 – 189, (2005).
- [30] M.H. Kuok, S.C. Ng, V.L. Zhang, *Angular dispersion of surface acoustic waves on (001), (110), and (111) GaAs*, J. Appl. Phys. 89, 7899–7902 (2001).
- [31] S. Neogi, J. S. Reparaz, L. F. C. Pereira, et al., *Tuning Thermal Transport in Ultrathin Silicon Membranes by Surface Nanoscale Engineering*, ACS Nano, 9, 4, 3820–3828 (2015).
- [32] K. Kim, B. Song, V. Fernández-Hurtado, et al., *Radiative heat transfer in the extreme near field*. Nature 528, 387–391 (2015). <https://doi.org/10.1038/nature16070>.
- [33] D. Naumenko, R. Mincigrucchi, M. Altissimo, et al., *Thermoelasticity of nanoscale silicon carbide membranes excited by extreme ultraviolet transient gratings: implications for mechanical and thermal management*, ACS Appl. Nano Mater. 2, 5132 (2019).
- [34] D. Fainozzi, F. Caporaletti, F. Capotondi, et al., *Temperature effects on the nanoscale thermoelastic response of a SiO₂ membrane*, APL Mater. 12, 051122 (2024).
- [35] Klas, R., Kirsche, A., Gebhardt, M. et al., *Ultra-short-pulse high-average-power megahertz-repetition-rate coherent extreme-ultraviolet light source*, Photonix 2, 4 (2021). <https://doi.org/10.1186/s43074-021-00028-y>
- [36] J. Cuffe, O. Ristow, E. Chavez, et al., *Lifetimes of Confined Acoustic Phonons in Ultrathin Silicon Membranes*, Physical Review Letter, 110, 095503 (2013).

-
- [37] K. Kunal and N. R. Aluru, *Akhiezer damping in nanostructures*, Physical Review B 84, 245450 (2011).
- [38] D. Van Thourhout and J. Roels, *Optomechanical device actuation through the optical gradient force*, Nature Photon 4, 211–217 (2010). <https://doi.org/10.1038/nphoton.2010.72>
- [39] S. Rechnitz, T. Tabachnik, M. Shlafman, et al., *Mode coupling bi-stability and spectral broadening in buckled carbon nanotube mechanical resonators*, Nat Commun 13, 5900 (2022). <https://doi.org/10.1038/s41467-022-33440-4>
- [40] B. Ilic, Y. Yang, K. Aubin, et al., *Enumeration of DNA Molecules Bound to a Nanomechanical Oscillator*, Nano Lett. 5, 925 (2005).
- [41] Y. Hwang, J. Puebla, K. Kondou, et al., *Strongly Coupled Spin Waves and Surface Acoustic Waves at Room Temperature*, Physical Review Letter 132, 056704 (2024).
- [42] M. Küß, M. Heigl, L. Flacke, et al., *Nonreciprocal Dzyaloshinskii–Moriya Magnetoacoustic Waves*, Physical Review Letter 125, 217203 (2020).
- [43] N.K.P. Babu, A. Trzaskowska, P. Graczyk, et al., *The Interaction between Surface Acoustic Waves and Spin Waves: The Role of Anisotropy and Spatial Profiles of the Modes*, Nano Lett., 21, 946–951 (2021).

Broadband surface phonon spectroscopy by time-domain extreme ultraviolet diffuse scattering

Supplementary Material

F.Capotondi^{1,*}, A.Maznev², F.Bencivenga¹, S.Bonetti³, D.Fainozzi¹, D.Fausti¹, L.Foglia¹, C.Gutt⁴, N.Jaouen⁵, D.Ksenzov⁴, C.Masciovecchio¹, K.A.Nelson², I.Nikolov¹, M.Pancaldi^{1,3}, E.Pedersoli¹, B.Pfau⁶, L.Raimondi¹, F.Romanelli⁷, R.Totani¹, M. Trigo⁸

¹ Elettra Sincrotrone Trieste, Strada Statale 14, km 163.5, 34149 Basovizza, TS, Italy.

² Massachusetts Institute of Technology Cambridge, Massachusetts 02139, USA.

³ Department of Molecular Sciences and Nanosystems, Ca' Foscari University of Venice, Venice, Italy

⁴ Universität Siegen, Walter-Flex-Strasse 3, 57072 Siegen, Germany.

⁵ Synchrotron SOLEIL, Saint-Aubin, Boite Postale 48, 91192, Gif-sur-Yvette Cedex, France.

⁶ Max Born Institute, Max-Born-Straße 2A, 12489 Berlin, Germany.

⁷ Department of Mathematics and Geosciences, University of Trieste, Trieste, Italy

⁸ SLAC National Accelerator Laboratory, Menlo Park, CA, USA.

S1. Data Analysis

To extract surface phonon information from Extreme ultraviolet Diffuse Scattering (EDS), four different images were collected under different illumination conditions:

- one signal image ($I_{FEL+Laser}$), collected at a fixed delay with both the free electron laser (FEL) and pump laser illuminating the sample surface;
- one laser background image ($I_{BG Laser}$), collected with only the optical laser active to account for optical stray radiation reaching the CCD detector;
- one signal image (I_{FEL}), collected with only the FEL illumination;
- one dark background image (I_{BG}), collected without any radiation inside the experimental chamber to measure the CCD detector's readout noise level.

For each signal image, background correction was performed as follows: for the pumped image, the background was removed considering $I_{pumped} = I_{FEL+Laser} - I_{Laser}$; for the static image, it was $I_{static} = I_{FEL} - I_{BG}$. The resulting background-free images were then normalized with respect to the total FEL intensity measured by the beamline photon transport monitor, and the two normalized images were subtracted to highlight the variations in scattered intensity due to phonon dynamics. Additionally, a pixel-by-pixel renormalization relative to the static image intensity was applied, as detailed in equation (1) of the main article.

Finally, an isomorphic transformation was applied to correct for the stereographic projection of the diffraction pattern onto the flat CCD plane and the nonlinear coordinate warping caused by the angle between the specimen and the detector [1,2]. Figure S1 (a) and S1(b) illustrate this correction: Figure S1(a) shows the EDS data as collected on the CCD chip, while Figure S1(b) displays the corrected data in the (Q_x, Q_y) plane. During a dynamical temporal scan, the images I_{FEL} and I_{BG} used for defining the static sample diffuse scattering were collected every 10 temporal points.

After applying the geometrical correction, the radial average shown in Figure S1(b) is obtained by integrating the scattered intensity over the azimuthal angle at a given $Q = \sqrt{Q_x^2 + Q_y^2}$ from the center of the image (blue trace in Figure S1(c)). To account for low-frequency quasi-DC offset between different collected frames, which may arise from temporal drifts in CCD background noise or residual laser stray light, a second-order polynomial background (dashed red line in Figure S1(c)) was subtracted from the radial average data. This adjustment ensures that the final $S(Q, \Delta t)$ map accurately reflects the variations induced by phonon dynamics.

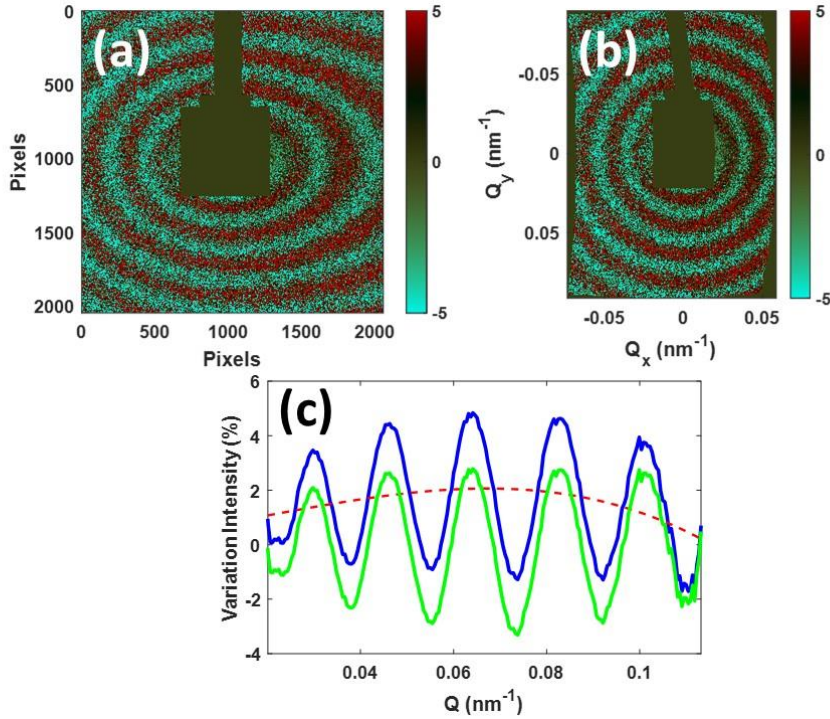


Figure S1. (a) Differential EDS images captured in the CCD chip frame with a sample-to-detector angle of 45° , showing oval distortion in the horizontal plane of the intensity modulation. (b) Differential EDS images after applying stereographic correction, represented in the (Q_x, Q_y) plane. (c) Azimuthal average of the data shown in panel (b) as a function of exchanged momentum Q (blue line). The dashed red line represents the low-frequency second-order polynomial background correction applied to account for residual signal noise from CCD electronics and/or stray radiation from the pump laser. The offset-compensated green trace for each time frame is finally used to construct the $S(Q, \Delta t)$ map.

Figure S2 compares the azimuthal radial average map $S(Q, \Delta t)$ without (Figure S2(a)) and with (Figure S2(b)) low-frequency quasi-DC offset subtraction for the $[\text{Pt}(4\text{nm})/\text{Al}(4\text{nm})]_4$ multilayer stack grown on Si/SiO_2 substrate presented in the main text (Figure 2). This figure demonstrates that the line-by-line second-order polynomial background correction introduces minimal perturbation in the primary output of the data analysis - namely, the dispersion of the SAWs phonon mode - which is shown for both cases in panels Figure S2(c) and Figure S2(d), respectively. As shown in panel Figure S2(a), the line-by-line low-frequency quasi-DC offset correction effectively removes spurious intensity biases in the data analysis, such as intensity jumps likely caused by background noise fluctuations in the CCD detector, particularly in the 400 – 500 ps and 600 – 700 ps ranges.

It is important to note that, while this procedure effectively eliminates background fluctuations in the experimental data, it may introduce artifacts near time zero (i.e., the moment of optical laser and FEL pulse overlap) and during the first few tens of picoseconds of SAW dynamic, when the fringe pattern in the detector plane is not fully developed and/or the first few ring structures are recorded. This effect is particularly relevant for low-scattering samples with smooth surfaces. However, once the ring structure is well developed within the detector's field of view, the impact of these potential artifacts diminishes. Additionally, since the phonon dispersion curve is retrieved by applying a Fourier transform to the full dataset, any residual artifacts have a negligible effect on the final estimate of the surface phonon velocity.

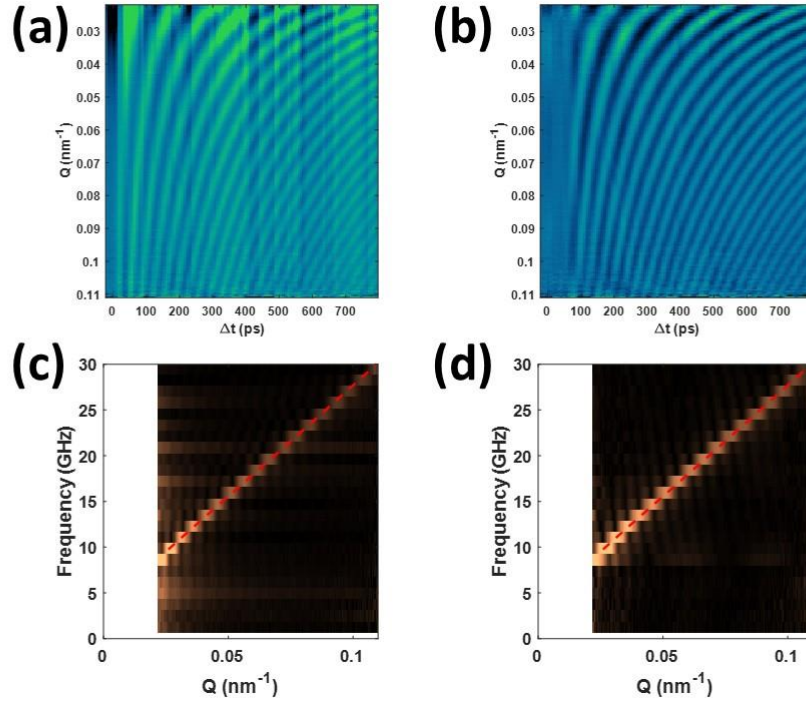


Figure S2. Azimuthal radial average map $S(Q, \Delta t)$ as a function of Q and Δt for the $[\text{Pt}(4\text{nm})/\text{Al}(4\text{nm})]_4$ multilayer stack on a Si/SiO_2 substrate without (a) - and with (b) - the line by line low frequency quasi-DC offset correction. (c) – (d) Fourier transform of the data in panels (a) and (b) respectively; the dashed red line highlights the linear dispersion of the oscillation frequency vs phonon wavevector (Q).

S2. EUV diffuse scattering on additional samples

To further explore the general applicability of time-resolved EDS in probing surface wave phonon dynamics, this section presents additional $S(Q, \Delta t)$ maps and the corresponding dispersion curves for various samples measured during the experimental campaign. Each analysis is compared with surface roughness measurements obtained via atomic force microscopy (AFM). Table S1 details the experimental conditions for each sample, with all experiments conducted using a 395 nm optical laser pulse for excitation and probing the dynamics with extreme ultraviolet (EUV) FEL radiation at 17.8 nm.

Sample	Laser energy density (mJ/cm ²)	FEL energy density per shot (mJ/cm ²)	Total Number of input photons per acquisition	Total Number of recorded photons on CCD detectors	Surface scattering efficiency
Si/Co (75 nm)/Ta(2 nm)	12.6±0.3	0.83±0.02	2.1 ×10 ¹³	2.25±0.05 ×10 ⁹	1.07±0.02 ×10 ⁻⁴
Si/Ta (75 nm)	23.1±0.3	1.45±0.02	1.9 ×10 ¹³	1.38±0.05 ×10 ⁹	7.2±0.3 ×10 ⁻⁵
Si/Cr(7 nm)/Au(75 nm)	12.6±0.3	0.83±0.02	5.3 ×10 ¹²	7.6±0.1 ×10 ⁹	4.0±0.1 ×10 ⁻³
Si/Pt(50 nm)	23.2±0.3	1.51±0.04	3.8 ×10 ¹³	5.6±0.3 ×10 ⁹	1.47±0.07 ×10 ⁻⁴
Si ₃ N ₄ /Pt(50 nm)	23.2±0.3	1.46±0.04	3.8 ×10 ¹³	1.8±0.1 ×10 ¹⁰	4.6±0.3 ×10 ⁻⁴
Si	52.8±0.7	0.90±0.02	3.5×10 ¹³	5.7±0.3 ×10 ⁷	1.63±0.05 ×10 ⁻⁶
Ge	6.75±0.05	0.72±0.01	4.5×10 ¹³	6.6±0.2 ×10 ⁸	1.46±0.04 ×10 ⁻⁵

Table S1. Experimental conditions used during the time resolved EDS experiments for different samples.

Figures S3, S5, S7, S9, S11, S13, and S15 present the AFM images of all the additional samples. The surface roughness σ_R of these samples ranges from 0.2 nm (bulk Si) to 2.5 nm (Au thin film), with typical correlation lengths (Λ), defined as the distance at which the autocorrelation function decays to $1/e$ of its initial value [3], spanning several tens of nanometers. Time-dependent $S(Q, \Delta t)$ intensity maps and the corresponding Fourier analysis for SAW phonon dispersion are shown for each sample in Figures S4, S6, S8, S10, S12, S14, and S16.

Table S2 summarizes the morphological properties of the surface samples and the inferred propagation velocities of the excited surface waves. These velocities are compared with the Rayleigh wave velocity (V_R) calculated using the formula ($V_R = V_S \frac{0.862+1.14\nu}{1+\nu}$), where V_S is the shear-wave velocity and ν is the Poisson ratio, based on data from the literature.

Sample	σ_R (nm)	Λ (nm)	V_R measured (m/s)	V_R from literature (m/s)
Si/Co (75 nm)/Ta(2 nm)	0.67	11±1	2530	2710 [4]
Si/Ta (75 nm)	0.76	9±1/6±1	1820	1870 [5]
Si/Cr(7 nm)/Au(75 nm)	2.50	33±5	850	1100 [6,7]
Si/Pt(50 nm)	0.6	10±1	1330	1670 [6,7]
Si ₃ N ₄ /Pt(50 nm)	1.1	12±2/8±2	1380	1670 [6,7]
Si	0.2	18±2	5210	5400 [8]
Ge	0.4	22±2	3120	3200 [9]

Table S2. Surface roughness of various samples as inferred from AFM image analysis, along with a comparison of the measured surface wave propagation velocities to values reported in the literature.

For sake of completeness, Figures S17, S18 and S19 report the AFM images of the sample presented in the main text, i.e. a [Pt(4nm)/Al(4nm)]₄ multilayer stack grown on a Si/SiO₂ substrate, a (001) oriented GaAs crystal and a 100 nm thick Ti layer on a Si substrate, respectively.

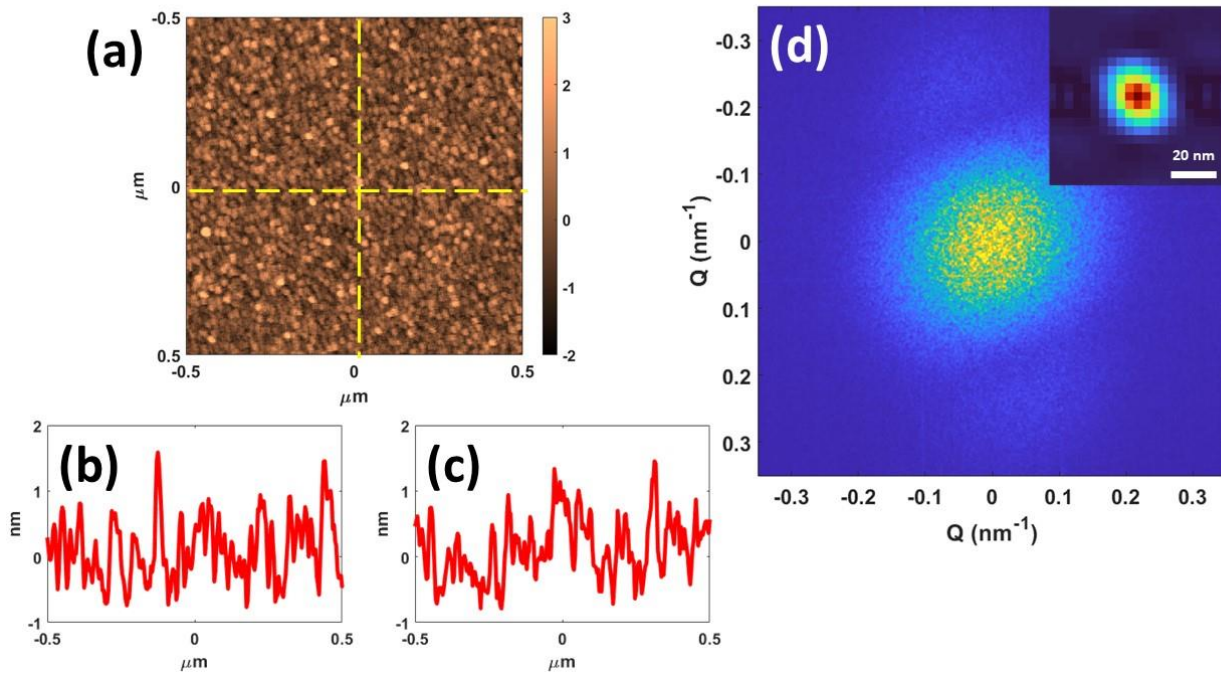


Figure S3. (a) $1 \times 1 \mu\text{m}^2$ AFM image of Si/Co (75 nm)/Ta(2 nm) sample, where the 2 nm Ta top layer was deposited to prevent Co oxidation. (b) and (c) display representative horizontal and vertical profiles along the dashed yellow line in panel (a). Statistical analysis of these height profiles yields a σ_R of about 0.67 nm. (d) shows the Fourier transform of the AFM image. The top-right inset displays the central part of the autocorrelation function, revealing a nearly isotropic roughness correlation length of 11 ± 1 nm.

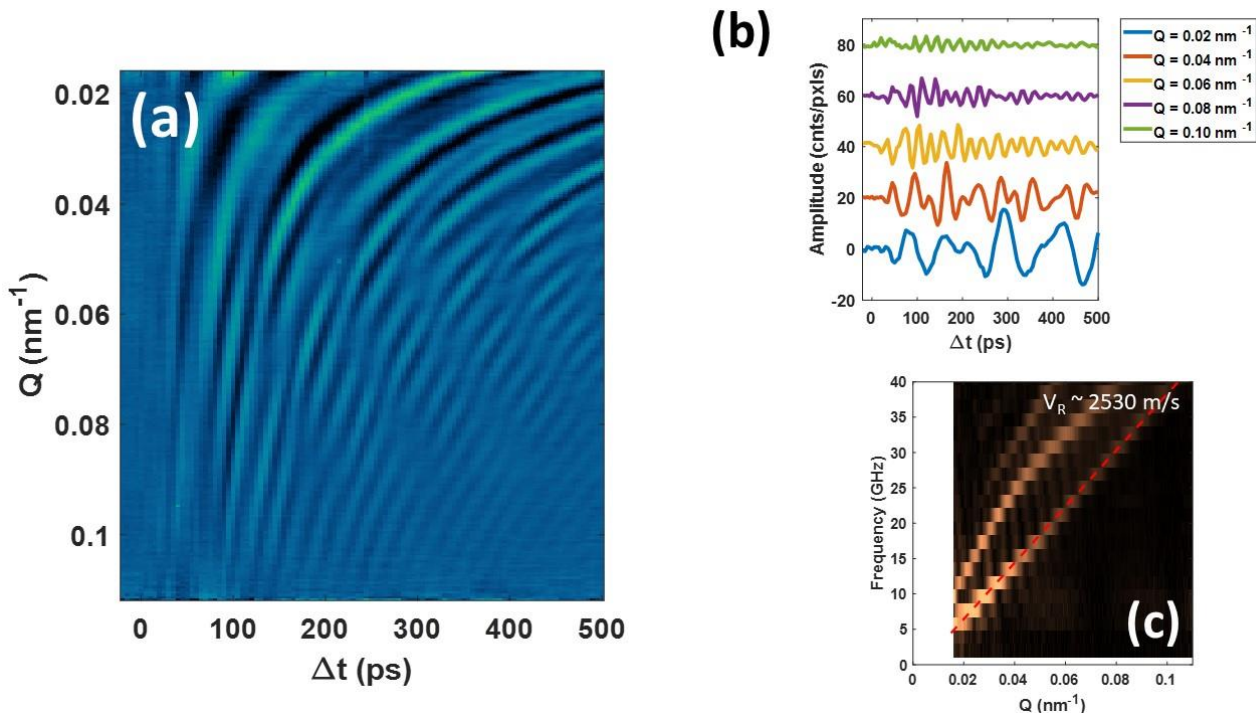


Figure S4. (a) Azimuthally averaged differential diffuse scattering intensity $S(Q, \Delta t)$ as a function of Q and Δt for the Si/Co (75 nm)/Ta(2 nm) sample on a Si substrate. (b) Time dependence of $S(Q, \Delta t)$ at selected values of Q in the range $0.02 - 0.10 \text{ nm}^{-1}$. (c) Fourier transform of the data in panel (a), with the dashed red line indicating the linear dispersion of the first Rayleigh mode, corresponding to a surface phonon propagation velocity of $2530 \pm 50 \text{ m/s}$.

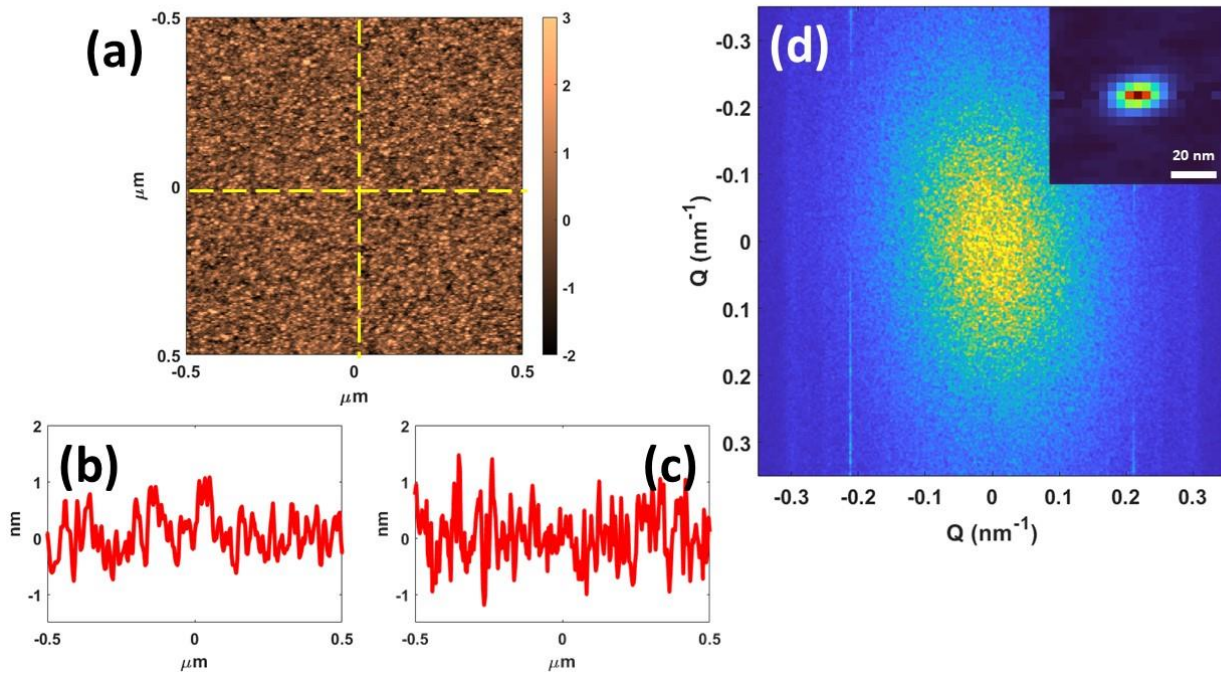


Figure S5. (a) $1 \times 1 \mu\text{m}^2$ AFM image of Si/Ta (75 nm) sample. (b) and (c) display representative horizontal and vertical profiles along the dashed yellow line in panel (a). Statistical analysis of these height profiles yields a σ_R of about 0.76 nm. (d) shows the Fourier transform of the AFM image. The top-right inset provides the central part of the autocorrelation function, revealing an anisotropic correlation length of 9 ± 1 nm in horizontal direction and 6 ± 1 nm in vertical direction.

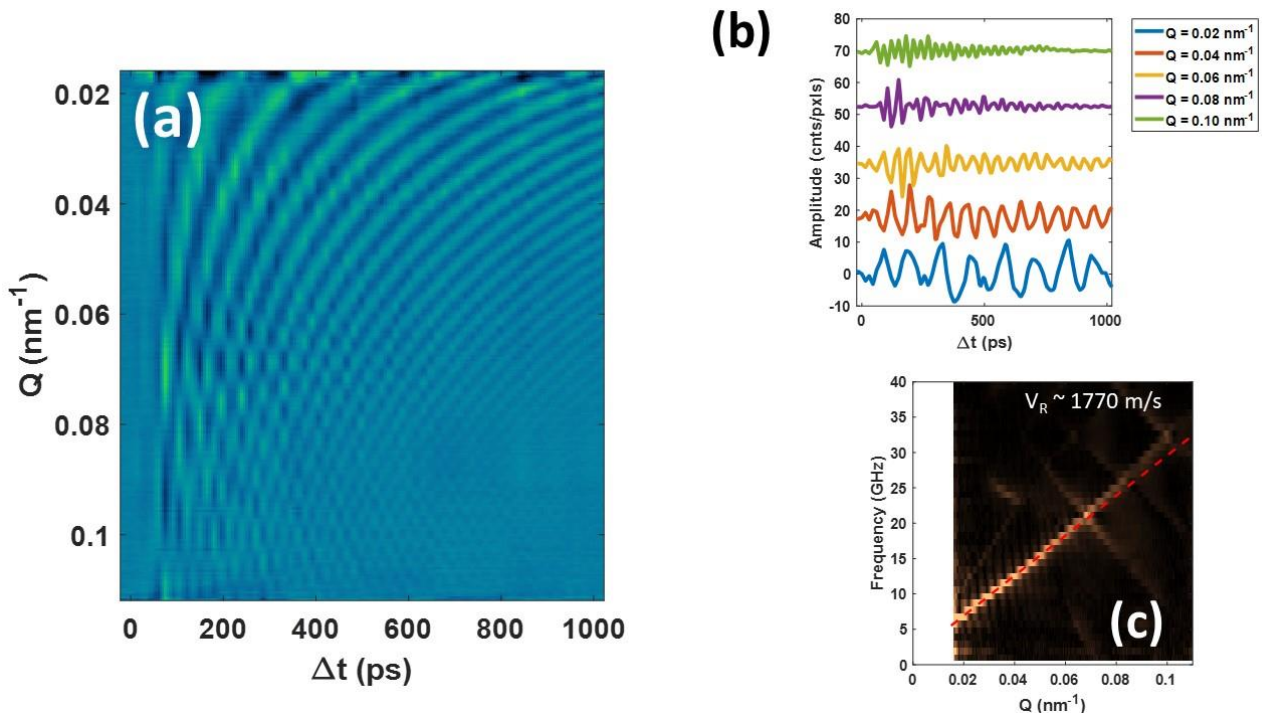


Figure S6. (a) Azimuthally averaged differential diffuse scattering intensity $S(Q, \Delta t)$ as a function of Q and Δt for the Si/Ta (75 nm) sample. (b) Time dependence traces at selected values of Q in the range $0.02 - 0.10 \text{ nm}^{-1}$. (c) Fourier transform of the data in panel (a), with the dashed red line indicating the linear dispersion of the first Rayleigh mode, corresponding to a surface phonon propagation velocity of $1820 \pm 50 \text{ m/s}$.

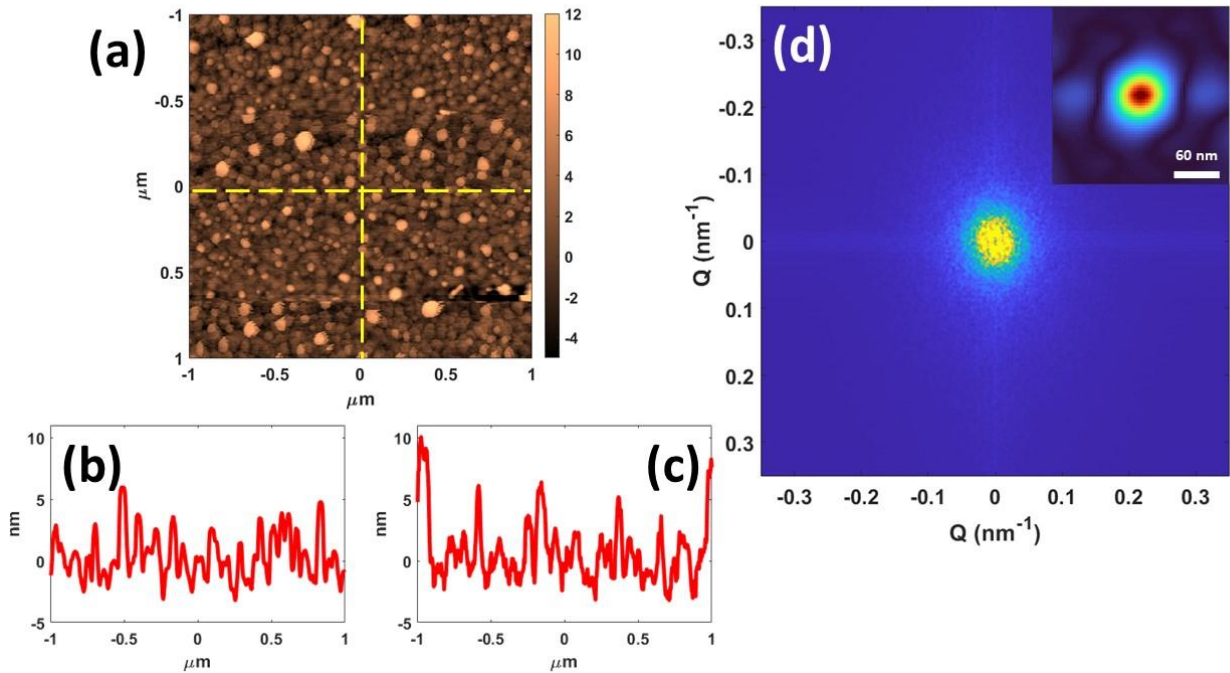


Figure S7. (a) $2 \times 2 \mu\text{m}^2$ AFM image of Si/Cr(7 nm)/Au(75 nm) sample. The 7 nm Cr interlayer was deposited as an adhesion layer to facilitate the sputtering deposition of the Au film on the Si substrate. (b) and (c) display representative horizontal and vertical profiles taken along the dash yellow line in panel (a). Statistical analysis of these height profiles yields a σ_R of about 2.5 nm. (d) shows the Fourier transform of the AFM image. The top-right inset displays the central part of the autocorrelation function, revealing a nearly isotropic roughness correlation length of 33 ± 5 nm.

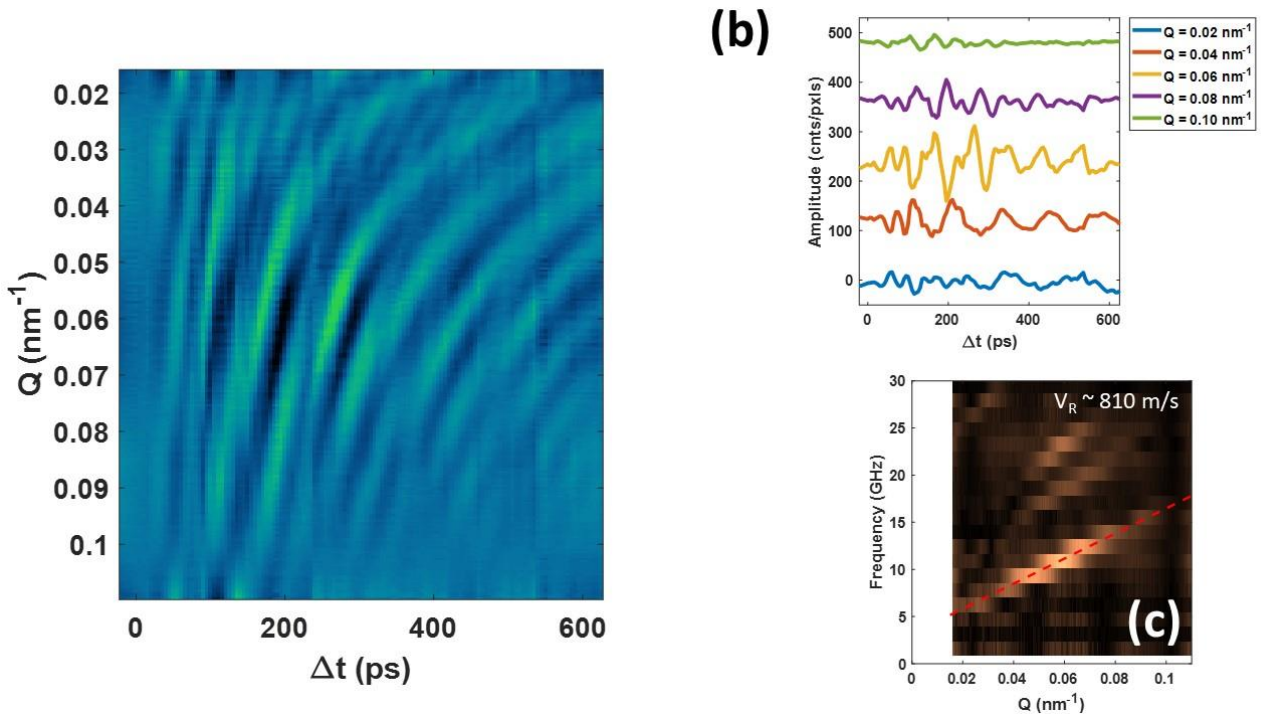


Figure S8. (a) Azimuthally averaged differential diffuse scattering intensity $S(Q, \Delta t)$ as a function of Q and Δt for the Si/Cr(7 nm)/Au(75 nm) sample. (b) Time dependence traces at selected values of Q in the range $0.02 - 0.10 \text{ nm}^{-1}$. (c) Fourier transform of the data in panel (a), with the dashed red line indicating the linear dispersion of the first Rayleigh mode, corresponding to a surface phonon propagation velocity of 850 ± 50 m/s.

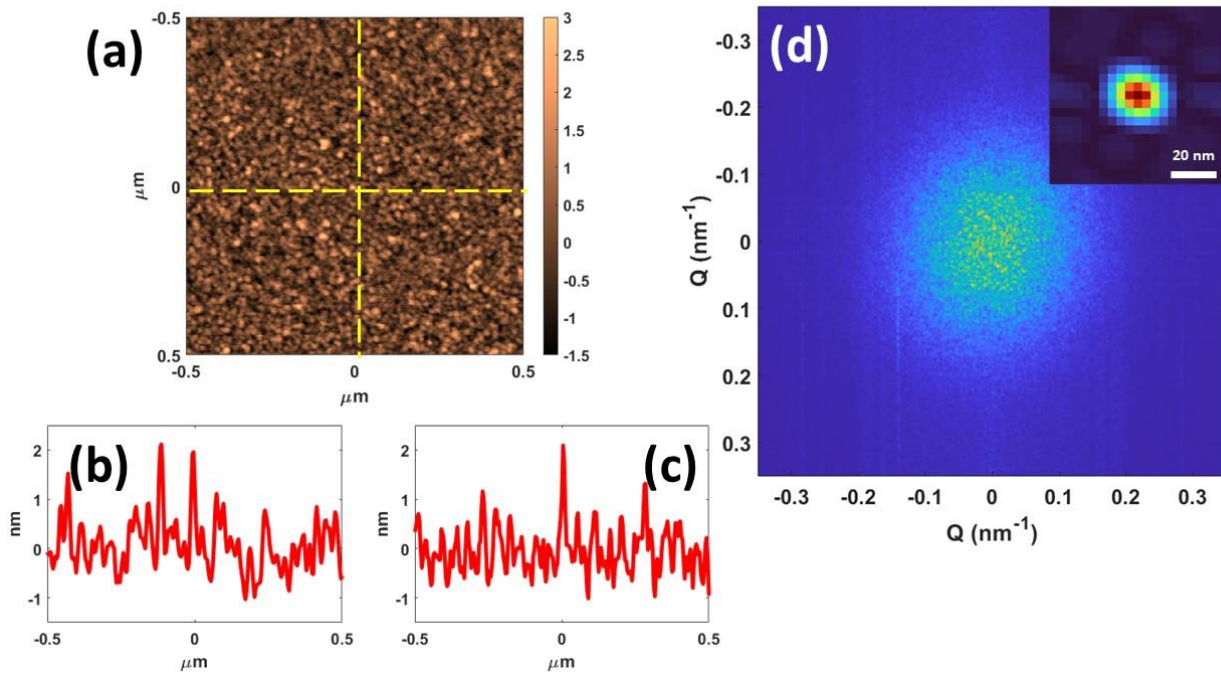


Figure S9. (a) $1 \times 1 \mu\text{m}^2$ AFM image of Si/Pt(50 nm) sample. (b) and (c) display representative horizontal and vertical profiles taken along the dash yellow line in panel (a). Statistical analysis of these height profiles yields a σ_R of about 0.6 nm. (d) shows the Fourier transform of the AFM image. The top-right inset displays the central part of the autocorrelation function, revealing a nearly isotropic roughness correlation length of 10 ± 1 nm.

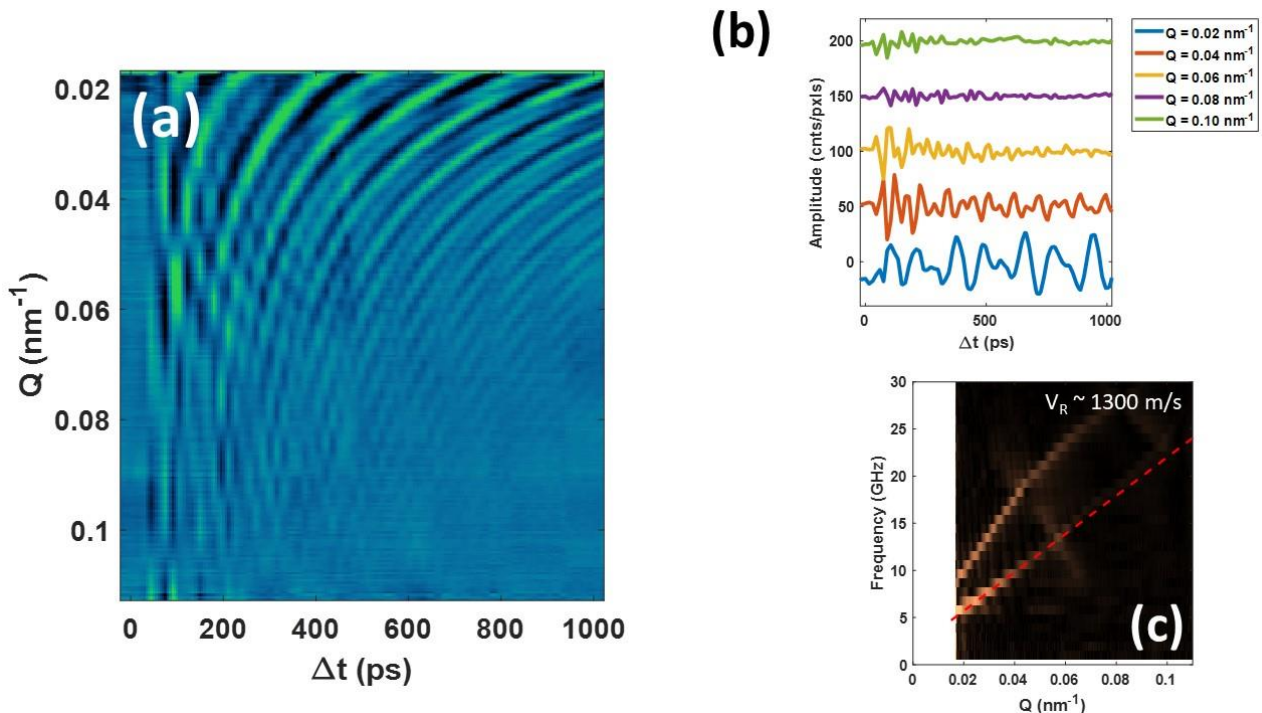


Figure S10. (a) Azimuthally averaged differential diffuse scattering intensity $S(Q, \Delta t)$ as a function of Q and Δt for the Si/Pt(50 nm) sample. (b) Time dependence traces at selected values of Q in the range $0.02 - 0.10 \text{ nm}^{-1}$. (c) Fourier transform of the data in panel (a), with the dashed red line indicating the linear dispersion of the first Rayleigh mode, corresponding to a surface phonon propagation velocity of $1330 \pm 50 \text{ m/s}$.

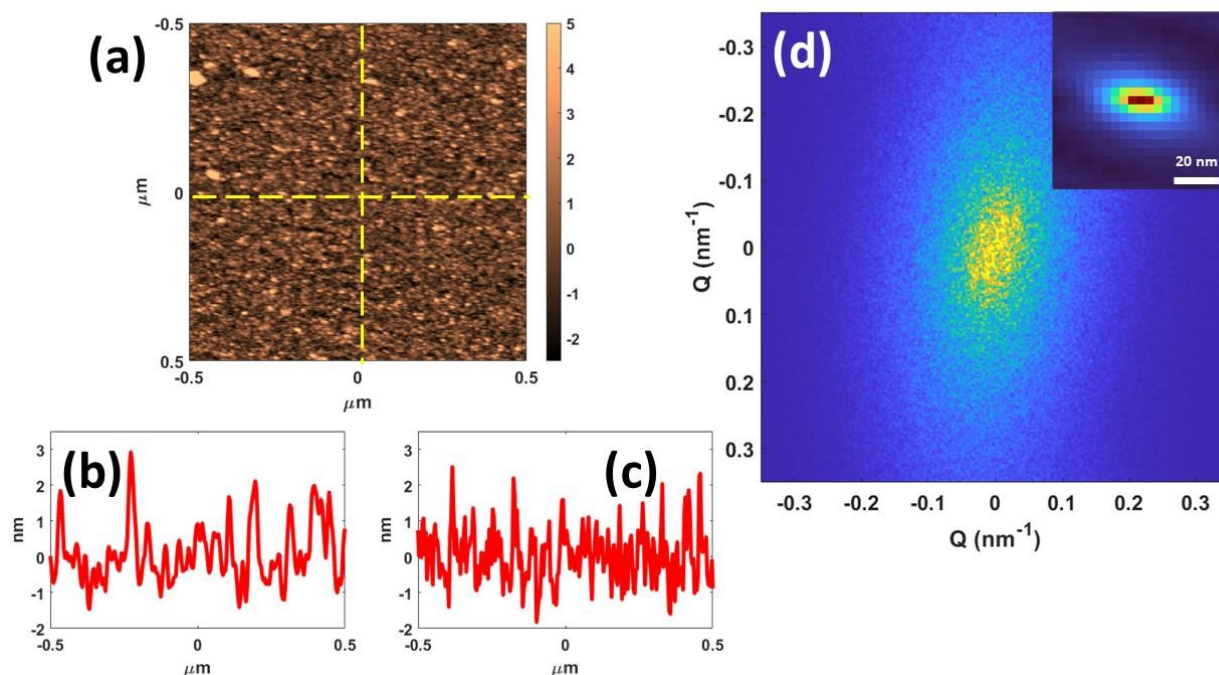


Figure S11. (a) $1 \times 1 \mu\text{m}^2$ AFM image of $\text{Si}_3\text{N}_4/\text{Pt}(50 \text{ nm})$ sample. (b) and (c) display representative horizontal and vertical profiles taken along the dash yellow line in panel (a). Statistical analysis of these height profiles yields a σ_R of about 1.1 nm. (d) shows the Fourier transform of the AFM image. The top-right inset provides the central part of the autocorrelation function, revealing an anisotropic correlation length of $12 \pm 2 \text{ nm}$ in horizontal direction and $8 \pm 2 \text{ nm}$ in vertical direction.

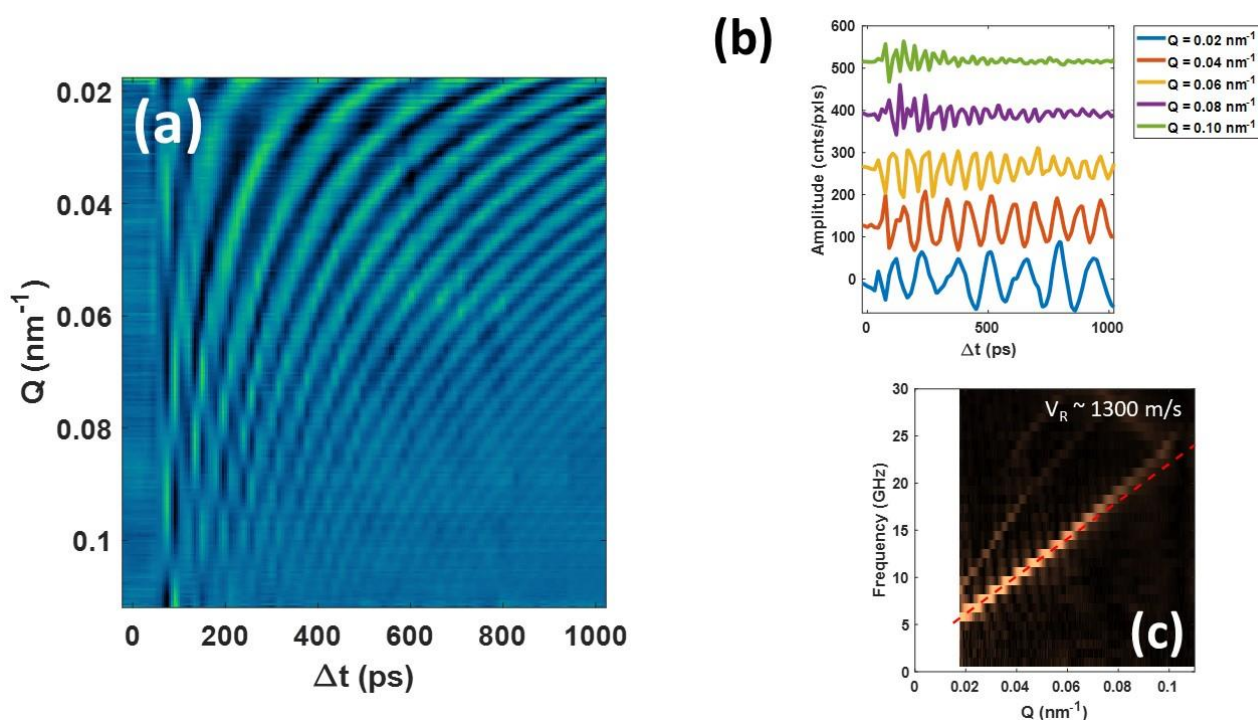


Figure S12. (a) Azimuthally averaged differential diffuse scattering intensity $S(Q, \Delta t)$ as a function of Q and Δt for the $\text{Si}_3\text{N}_4/\text{Pt}(50 \text{ nm})$ sample. (b) Time dependence traces at selected values of Q in the range $0.02 - 0.10 \text{ nm}^{-1}$. (c) Fourier transform of the data in panel (a), with the dashed red line indicating the linear dispersion of the first Rayleigh mode, corresponding to a surface phonon propagation velocity of $1380 \pm 50 \text{ m/s}$.

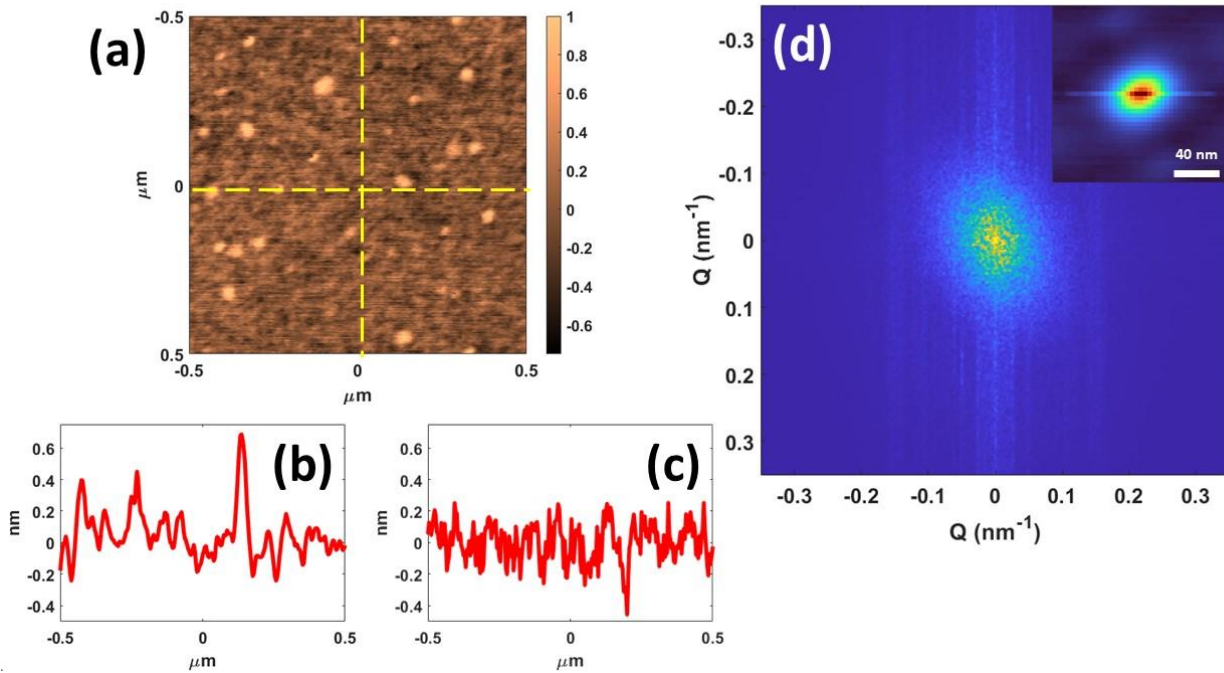


Figure S13. (a) $1 \times 1 \mu\text{m}^2$ AFM image of Si sample. (b) and (c) display representative horizontal and vertical profiles taken along the dash yellow line in panel (a). Statistical analysis of these height profiles yields a σ_R of about 0.18 nm. (d) shows the Fourier transform of the AFM image. The top-right inset displays the central part of the autocorrelation function, revealing a nearly isotropic roughness correlation length of 18 ± 2 nm.

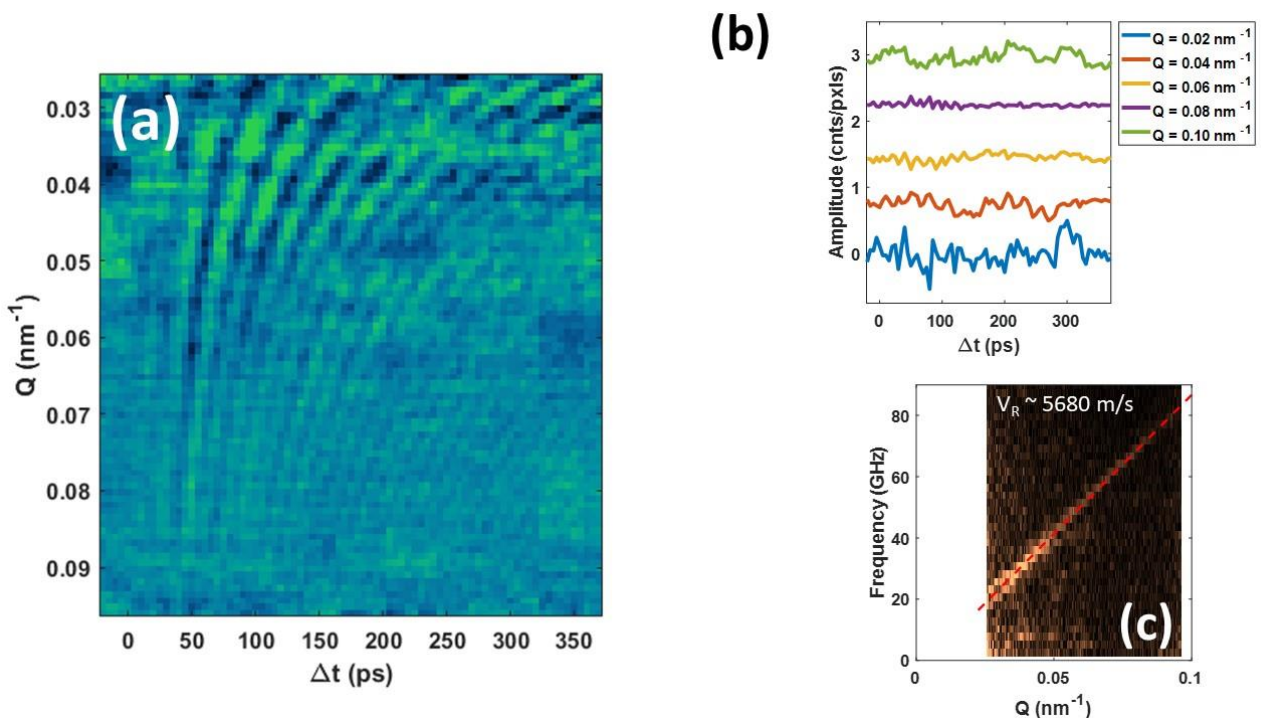


Figure S14. (a) Azimuthally averaged differential diffuse scattering intensity $S(Q, \Delta t)$ as a function of Q and Δt for the Si bulk sample. (b) Time dependence traces at selected values of Q in the range 0.03 – 0.07 nm^{-1} . (c) Fourier transform of the data in panel (a), with the dashed red line indicating the linear dispersion of the first Rayleigh mode, corresponding to a surface phonon propagation velocity of 5210 ± 50 m/s.

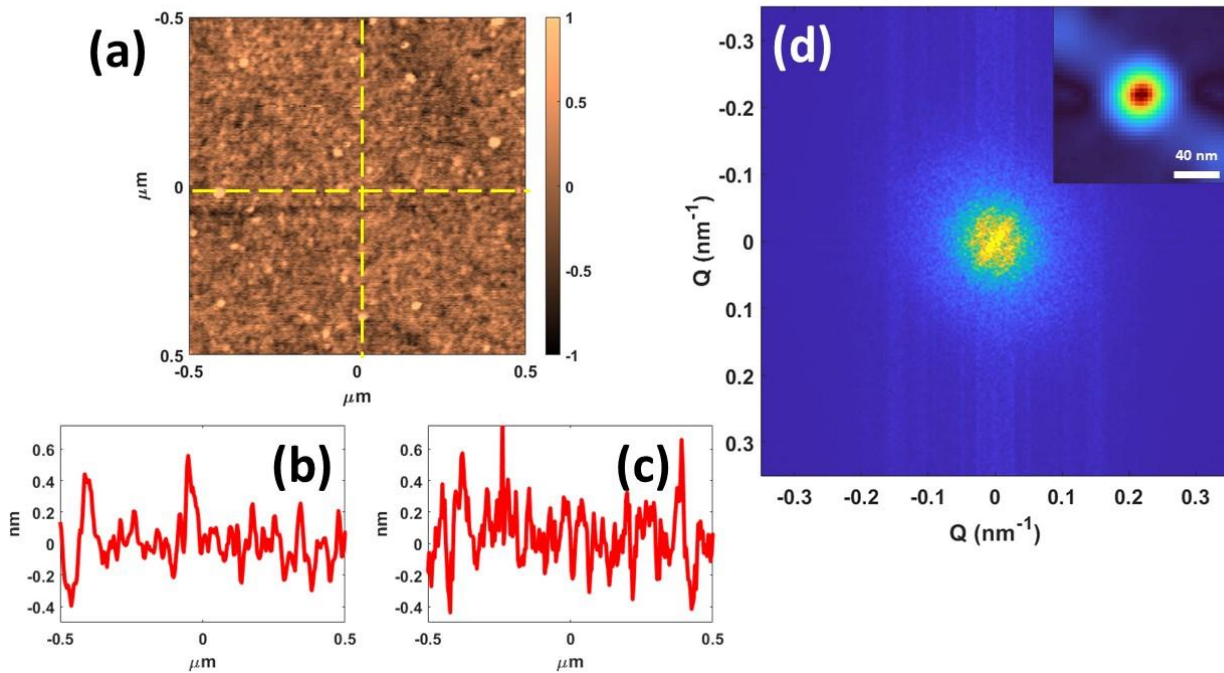


Figure S15. (a) $1 \times 1 \mu\text{m}^2$ AFM image of Ge sample. (b) and (c) display representative horizontal and vertical profiles taken along the dash yellow line in panel (a). Statistical analysis of these height profiles yields a σ_R of about 0.35 nm. (d) shows the Fourier transform of the AFM image. The top-right inset displays the central part of the autocorrelation function, revealing a nearly isotropic roughness correlation length of 20 ± 2 nm.

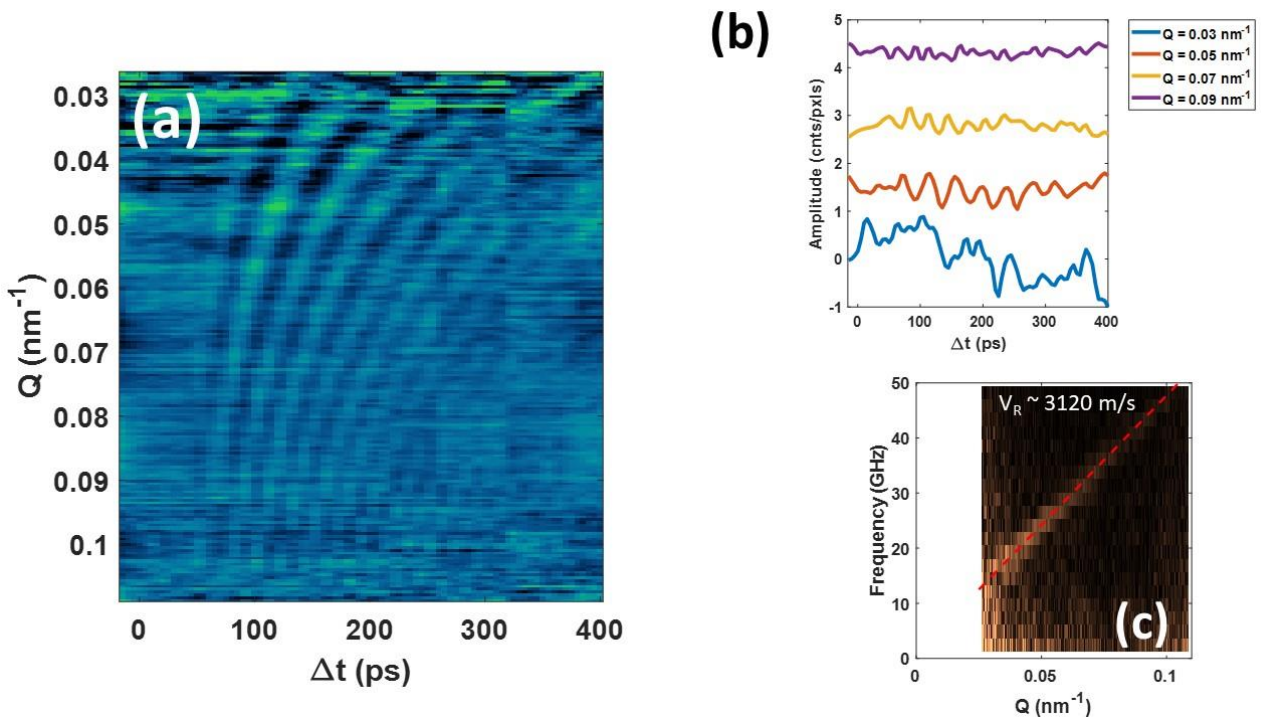


Figure S16. (a) Azimuthally averaged differential diffuse scattering intensity $S(Q, \Delta t)$ as a function of Q and Δt for the Ge bulk sample. (b) Time dependence traces at selected values of Q in the range 0.03 – 0.09 nm^{-1} . (c) Fourier transform of the data in panel (a), with the dashed red line indicating the linear dispersion of the first Rayleigh mode, corresponding to a surface phonon propagation velocity of 3120 ± 50 m/s.

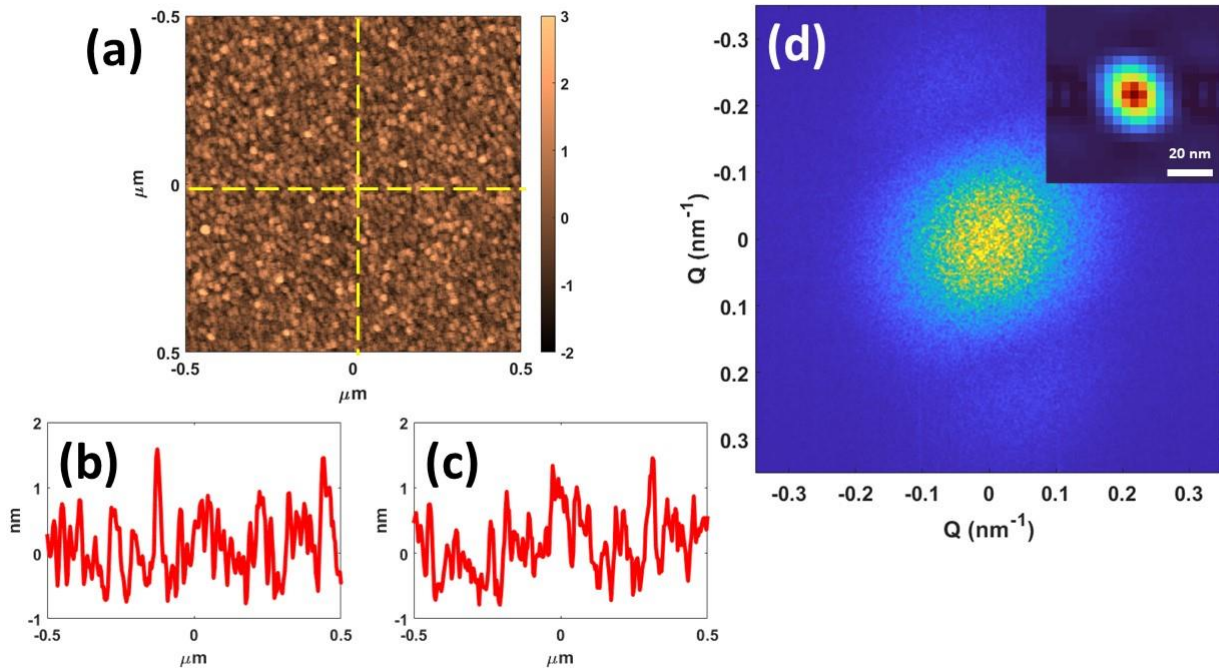


Figure S17. (a) $1 \times 1 \mu\text{m}^2$ AFM image of $[\text{Pt}(4\text{nm})/\text{Al}(4\text{nm})]_4$ multilayer stack grown on a Si/SiO₂ substrate. (b) and (c) display representative horizontal and vertical profiles taken along the dash yellow line in panel (a). Statistical analysis of these height profiles yields a σ_R of about 0.6 nm. (d) shows the Fourier transform of the AFM image. The top-right inset displays the central part of the autocorrelation function, revealing a nearly isotropic roughness correlation length of 14 ± 2 nm.

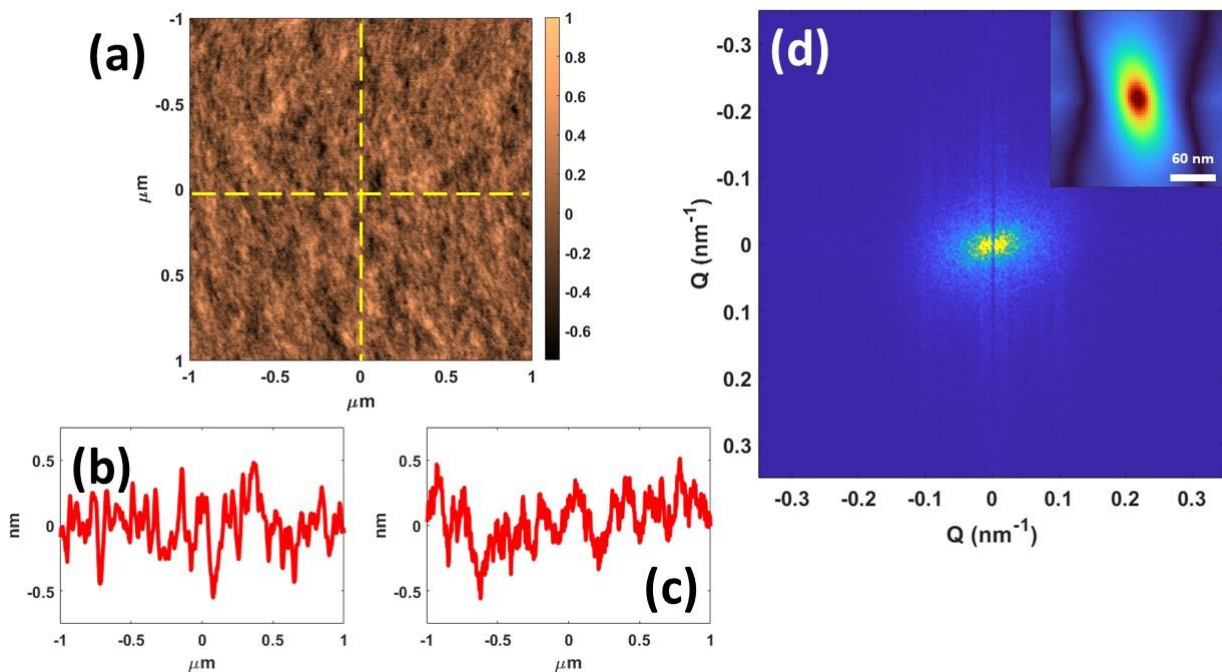


Figure S18. (a) $1 \times 1 \mu\text{m}^2$ AFM image of (001) oriented GaAs crystal. (b) and (c) display representative horizontal and vertical profiles taken along the dash yellow line in panel (a). Statistical analysis of these height profiles yields a σ_R of about 0.2 nm. (d) shows the Fourier transform of the AFM image. The top-right inset displays the central part of the autocorrelation function, revealing an anisotropic correlation length of 19 ± 2 nm in horizontal direction and 42 ± 5 nm in vertical direction.

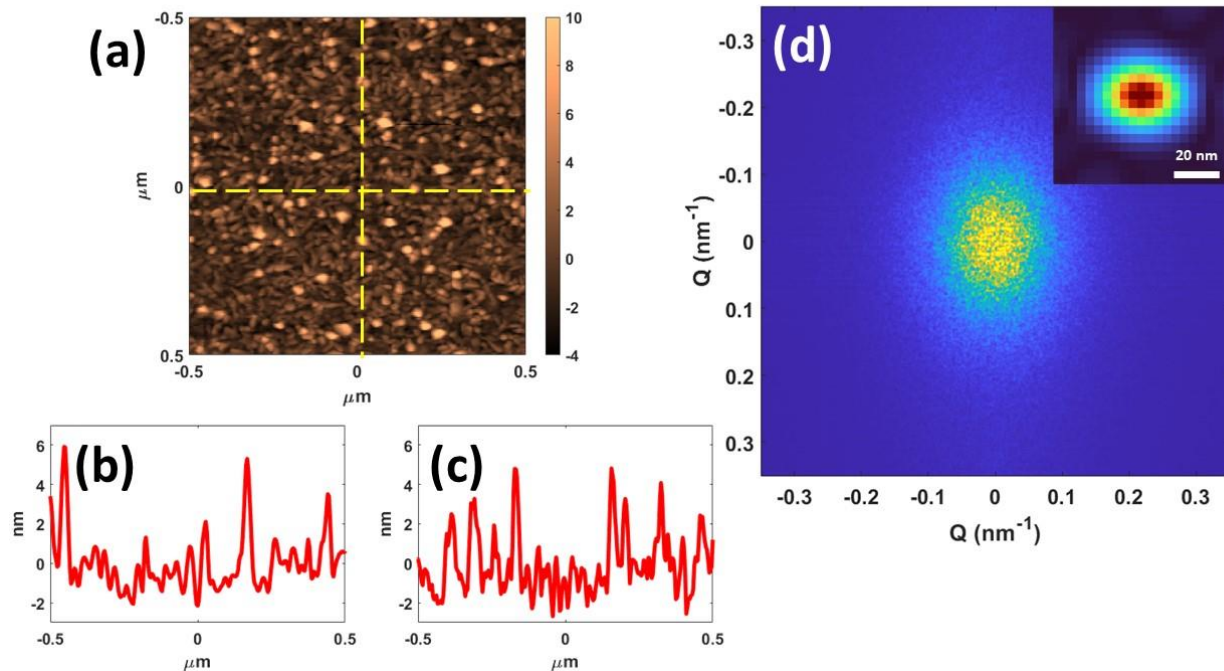


Figure S19. (a) $1 \times 1 \mu\text{m}^2$ AFM image of Si/Ti (100 nm) sample. (b) and (c) display representative horizontal and vertical profiles taken along the dash yellow line in panel (a). Statistical analysis of these height profiles yields a σ_R of about 2.0 nm. (d) shows the Fourier transform of the AFM image. The top-right inset displays the central part of the autocorrelation function, revealing a nearly isotropic roughness correlation length of 15 ± 2 nm.

REFERENCES

- [1] S. Schaffert, B. Pfau, J. Geilhufe, C. M. Günther, M. Schneider, C. von Korff Schmising, and S. Eisebitt, *High resolution magnetic-domain imaging by fourier transform holography at 21 nm wavelength*, New J. Phys. 15, 093042 (2013).
- [2] A. de Beurs, L. Loetgering, M. Herczog, M. Du, K. S. E. Eikema, and S. Witte *aPIE: an angle calibration algorithm for reflection ptychography*, Optics Letters 47, 8, 1949-1952 (2022).
- [3] K. Nagata, T. Umehara, J. Nishiwaki *The Determination of rms Roughness and Correlation Length of Rough Surface by Measuring Spatial Coherence Function* Jpn. J. Appl. Phys. 12 1693 (1973).
- [4] D. Antonangeli, M. Krisch, G. Fiquet, J. Badro, D. L. Farber, A. Bossak, and S. Merkel *Aggregate and single-crystalline elasticity of hcp cobalt at high pressure*, Physical Review B, 72, 134303 (2005).
- [5] D. Orlikowski, P. Söderlind, and J. A. Moriarty *First-principles thermoelasticity of transition metals at high pressure: Tantalum prototype in the quasiharmonic limit*, Physical Review B, 74, 054109 (2006).
- [6] A. Nayer, The Metals Databook, McGraw-Hill, New York, 1997.
- [7] R.B. Ross, Metallic Materials Specification Handbook, Fourth Ed., Chapman & Hall, London, 1992
- [8] S. Tamura, J. A. Shields and J. P. Wolfe, *Lattice dynamics and elastic phonon scattering in silicon*, Physical Review B, 44(7), 3001-3011 (1991).
- [9] A. Paul, M. Luisier, G. Klimeck, *Modified valence force field approach for phonon dispersion: from zinc-blende bulk to nanowires*. J Comput Electron 9, 160–172 (2010).